J. Fluid Mech. (2022), *vol*. 952, A18, doi:10.1017/jfm.2022.904

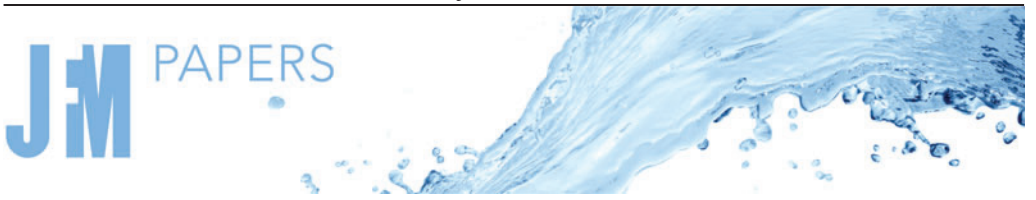

Revised mixing coefficient scaling for sheared stably stratified turbulence

Young R. Yi[1],† **and Jeffrey R. Koseff**[1]

[1]Bob and Norma Street Environmental Fluid Mechanics Laboratory, Department of Civil and Environmental Engineering, Stanford University, Stanford, CA 94305, USA

(Received 5 March 2022; revised 25 August 2022; accepted 25 October 2022)

We revisit and extend the turbulent Froude number (Fr_k) scaling for the mixing coefficient (Γ) introduced by Garanaik & Venayagamoorthy (GV) (*J. Fluid Mech.*, vol. 867, 2019, pp. 323–333) by directly incorporating the effects of mean shear through the non-dimensional shear parameter $S_* = Sk/\epsilon_k$. For flows where the effects of mean shear are stronger than the background vertical stratification, we find $\Gamma \sim Fr_k^{-2}S_*^{-1}$ for weakly stratified sheared turbulence and $\Gamma \sim Fr_k^{-1}S_*^{-1}$ for moderately stratified sheared turbulence. The scaling procedure is inconclusive for strongly stratified sheared turbulence, but using two independent datasets of homogeneous, sheared, stably stratified turbulence, we empirically observe $\Gamma \sim Fr_k^{-0.5}S_*^{-1}$. Our revised scaling better collapses both datasets compared with the original GV scaling, and we note that the moderately stratified sheared regime is extremely narrow (or maybe even non-existent). We also apply our scaling to the time-varying open channel simulations of Issaev *et al.* (*J. Fluid Mech.*, vol. 935, 2022) and observe $\Gamma \sim Fr_k^{-2}S_*^{-1}$ for weakly stratified sheared turbulence, but we observe deviations from our revised scaling for moderate and strong stratifications due to time-varying mean shear and vertical transport. Finally, we apply our revised scaling to field measurements of Conry, Kit & Fernando (*Environ. Fluid Mech.*, vol. 20, 2020, pp. 1177–1197) and observe $\Gamma \sim Fr_k^{-2}S_*^{-1}$. We emphasize that our revised scaling is applicable only for stably stratified, vertically sheared turbulence with weak spatio-temporal variations of the mean shear and stratification, and we expect different scaling to apply when additional effects such as depth-varying radiative heating/cooling are present or when the orientation of the mean shear relative to the gravity vector is modified (e.g. horizontal shear).

Key words: stratified flows, turbulent mixing, stratified turbulence

† Email address for correspondence: yryi@stanford.edu

1. Introduction

Oceanic flows are comprised of a vast range of spatio-temporal scales, but global ocean models only partially resolve this rich range of scales due to limited computational power (e.g. Fox-Kemper *et al.* 2019). Relatedly, their results have been shown to depend sensitively on how the subgrid-scale mixing of scalars and momentum are modelled (e.g. Bryan 1987; Jayne 2009), and in particular, great effort has been devoted to the accurate representation of the subgrid-scale vertical buoyancy flux because of its impact on the background density field as well as on the global ocean circulation through the buoyancy force (de Lavergne *et al.* 2015; Mashayek *et al.* 2017; Cimoli *et al.* 2019). The down-gradient model introduced by Osborn (1980) has been widely used to represent the subgrid-scale vertical buoyancy flux in global ocean models, and a non-dimensional form of this model from Salehipour & Peltier (2015) is provided below

$$\frac{D_T}{D} = \left(\frac{Ri_f}{1 - Ri_f}\right)\frac{\epsilon_k}{DN^2} = \Gamma\left(\frac{\epsilon_k}{\nu N^2}\right)\left(\frac{\nu}{D}\right) = \Gamma Re_b Pr. \tag{1.1}$$

In (1.1), D and D_T are the molecular and eddy diffusivities of density, ν is the kinematic viscosity of the fluid, N^2 is the vertical background stratification, ϵ_k is the rate of turbulent kinetic energy (TKE) dissipation, Ri_f is the flux Richardson number or mixing efficiency, $\Gamma = Ri_f/(1 - Ri_f)$ is the mixing coefficient, $Re_b = \epsilon_k/(\nu N^2)$ is the buoyancy Reynolds number and $Pr = \nu/D$ is the molecular Prandtl number.

By combining microstructure measurements of ϵ_k, conductivity-temperature-depth-based (CTD)-based measurements of N^2 and known values of ν and D, it is possible to estimate Re_b and Pr. Then, the final challenge with applying (1.1) to estimate the eddy diffusivity is quantifying Γ in terms of easily measurable and known quantities. There has been extensive research and discussion surrounding (1.1), and comprehensive summaries are provided in the review articles of Ivey, Winters & Koseff (2008), Gregg *et al.* (2018) and Caulfield (2020, 2021). Recently, one notable advancement has been provided by Maffioli, Brethouwer & Lindborg (2016), who showed that Γ depends primarily on the turbulent Froude number (Fr) and not the buoyancy Reynolds number (Re_b). The turbulent Froude number can be interpreted as a ratio of the buoyancy and eddy turnover time scales, and the buoyancy Reynolds number can be interpreted as the square of the ratio of the buoyancy and dissipation/Kolmogorov time scales. Maffioli *et al.* (2016) showed that $\Gamma \sim Fr^{-2}$ for weak stratification ($Fr \gg 1$) and $\Gamma \approx$ const. for strong stratification ($Fr \ll 1$), and hypothesized that the non-unique relationships of $\Gamma = f(Re_b)$ (e.g. figure 2 of Monismith, Koseff & White 2018) would be addressed when considering $\Gamma = g(Fr)$ (e.g. figures 14 and 6 of Issaev *et al.* 2022). Subsequently, Garanaik & Venayagamoorthy (2019) provided theoretical arguments for the relationships between Γ and Fr, where they introduced a third scaling regime for moderate stratification ($Fr \sim O(1)$) with $\Gamma \sim Fr^{-1}$. They tested these scaling relationships for Γ using three different direct numerical simulation (DNS) datasets of homogeneous stably stratified turbulence: (i) decaying simulations of Garanaik & Venayagamoorthy (2018); (ii) forced simulations of Maffioli *et al.* (2016); (iii) sheared simulations of Shih *et al.* (2005). The decaying and forced simulations exhibited great agreement with their theoretical scaling regimes. Nevertheless, the sheared dataset of Shih *et al.* (2005) did not visually exhibit the same degree of agreement with the scaling as a function of Fr as the two unsheared datasets (see figure 1 of Garanaik & Venayagamoorthy 2019).

To better understand this discrepancy between the mixing coefficient scaling relationships for unsheared and sheared, stably stratified turbulence, we revisit the theoretical arguments of Garanaik & Venayagamoorthy (2019), hereafter referred to as GV.

Specifically, for flows where the shear time scale $\tau_S \sim 1/S$ is faster than the buoyancy time scale $\tau_B \sim 1/N$, we introduce modifications to the GV scaling such that Γ depends on both the non-dimensional shear parameter $S_* = Sk/\epsilon_k$ and the turbulent Froude number $Fr_k = \epsilon_k/(Nk)$, where $\tau_L \sim k/\epsilon_k$ is the large-eddy time scale. We then validate our revised scaling relationships using two independent datasets of homogeneous, sheared, stably stratified, turbulence (one dataset from Shih *et al.* (2005); another dataset generated based on equations and methods outlined in § 3). We note that Mater & Venayagamoorthy (2014*a*,*b*) have also explored a two-parameter description of stably stratified turbulence using the two variables, $S\tau_L \sim S_*$ and $N\tau_L \sim 1/Fr_k$.

Our paper is organized as follows. In § 2, we provide an overview of the GV scaling procedure and introduce modifications to account for mean shear. In § 3, we introduce the equations of motion and describe the solution methods that were used to generate a second database of homogeneous, sheared, stably stratified turbulence and compare the resulting turbulence of this new shear-forced model problem with homogeneous shear flows. In § 4, we test and validate our revised scaling using two DNS datasets of homogeneous, sheared, stably stratified turbulence (one by Shih *et al.* (2005); another described in § 3), and test the applicability of our revised scaling for more complex sheared, stably stratified turbulent flows using two additional datasets (DNS of spatio-temporally evolving, radiatively heated, stably stratified, open channel flow by Issaev *et al.* (2022); field measurements of stably stratified atmospheric boundary-layer turbulence studied by Conry, Kit & Fernando 2020). We also explore the relationship between our revised scaling regimes and existing descriptions of the mixing efficiency based on the gradient Richardson number and briefly examine the effects of finite Reynolds number of the simulations on the mixing efficiency. In § 5, we close with a few concluding remarks.

2. Original and revised GV scaling arguments

2.1. *Recap of the GV mixing coefficient scaling relationships*

Before considering the effects of mean shear, we first summarize the turbulent Froude number (Fr_k) scaling relationships for the mixing coefficient (Γ) from Garanaik & Venayagamoorthy (2019) (see table 1 for a summary of the GV scaling). Given the Osborn eddy diffusivity model for the vertical buoyancy flux (1.1), the GV scaling procedure seeks to model the mixing coefficient $\Gamma = B/\epsilon_k$ for three regimes of stably stratified turbulence: (i) weak stratification ($Fr_k > 1$), (ii) moderate stratification ($Fr_k \sim O(1)$) and (iii) strong stratification ($Fr_k < 1$). Here, we use $Fr_k = \epsilon_k/(Nk)$ rather than $Fr = \epsilon_k/(Nu_{rms}^2)$, where k represents the TKE, and u_{rms} represents the root-mean-square horizontal velocity fluctuations, to be consistent with the presentation of GV. When stratification increases, leading to increasingly damped vertical velocity fluctuations, we expect Fr_k and Fr to become similar in magnitude. For forced, axisymmetric, strongly stratified turbulence, $k = (u^2 + v^2 + w^2)/2 \approx (u^2 + v^2)/2 \approx u_{rms}^2$ (i.e. $Fr_k \approx Fr$), and for sheared, strongly stratified turbulence, $k = (u^2 + v^2 + w^2)/2 \approx u^2/2 \approx u_{rms}^2/2$ (i.e. $Fr_k \approx 2Fr$). In these expressions, u, v and w represent velocity fluctuations in the x-, y- and z-directions, respectively, with gravity acting in the z-direction.

The GV scaling estimates the vertical displacement of fluid parcels as $l_z \sim w\tau_1$, where w represents the vertical velocity fluctuations, and τ_1 represents a time scale connecting the vertical velocity fluctuations to the vertical displacement of fluid parcels. Next, the TKE dissipation rate is scaled as $\epsilon_k \sim w^2/\tau_2$, where τ_2 represents a time scale connecting the vertical component of the TKE to the TKE dissipation rate. Using the first scaling, density

	$Fr_k = \epsilon_k/(Nk) \sim \tau_B/\tau_L$	τ_1	τ_2	$\Gamma = B/\epsilon_k \sim N^2\tau_1\tau_2$
Weakly stratified	$Fr_k > 1$, $\tau_B > \tau_L$	τ_L	τ_L	$\Gamma \sim Fr_k^{-2}$
Moderately stratified	$Fr_k \sim O(1)$, $\tau_B \sim \tau_L$	τ_B	τ_L	$\Gamma \sim Fr_k^{-1}$
Strongly stratified	$Fr_k < 1$, $\tau_B < \tau_L$	τ_B	τ_B	$\Gamma \approx$ const.

Table 1. GV scaling for unsheared stably stratified turbulence.

fluctuations are scaled as $\rho \sim l_z d_z\bar{\rho} \sim w\tau_1 d_z\bar{\rho}$, and substituting this into the vertical buoyancy flux expression leads to $B = (g/\rho_0)\overline{w\rho} \sim w^2N^2\tau_1$, where $N^2 = -(g/\rho_0)d_z\bar{\rho}$ is the background vertical stratification. Combining the scaling for B and ϵ_k, the GV scaling for the mixing coefficient can be generally stated as

$$\Gamma = \frac{B}{\epsilon_k} \sim N^2\tau_1\tau_2, \tag{2.1}$$

where now physically appropriate τ_1 and τ_2 can be chosen for the three stably stratified turbulence regimes of interest. For weakly stratified turbulence, $\tau_1 \sim \tau_2 \sim \tau_L$. This leads to $\Gamma \sim (N\tau_L)^2 \sim Fr_k^{-2}$. For moderately stratified turbulence, the buoyancy time scale and large-eddy time scale have comparable magnitudes, so GV pick $\tau_1 \sim \tau_B$ and $\tau_2 \sim \tau_L$ to incorporate both time scales, resulting in $\Gamma \sim N\tau_L \sim Fr_k^{-1}$. For strongly stratified turbulence, $\tau_1 \sim \tau_2 \sim \tau_B$, which leads to $\Gamma \sim Fr_k^0 \approx$ const.

There are three alternatives for scaling the moderately stratified regime, which are not explicitly discussed by Garanaik & Venayagamoorthy (2019). These alternatives arise because $\tau_L \sim \tau_B$ for $Fr_k \sim O(1)$. First, we could have chosen $\tau_1 \sim \tau_L$ and $\tau_2 \sim \tau_B$. This also leads to $\Gamma \sim Fr_k^{-1}$, but based solely on scaling arguments, it cannot be distinguished from the choice made by GV. Second, we could have chosen $\tau_1 \sim \tau_2 \sim \tau_L$ and arrived at $\Gamma \sim Fr_k^{-2}$ as with the weakly stratified regime. Third, we could have chosen $\tau_1 \sim \tau_2 \sim \tau_B$ and arrived at $\Gamma \sim Fr_k^0 \approx$ const. as with the strongly stratified regime. We interpret this ambiguity as a consequence of this regime being a transition zone between weakly stratified and strongly stratified regimes, which is how this regime is described by Garanaik & Venayagamoorthy (2019).

2.2. *Revised mixing coefficient scaling relationships with mean shear*

Extending the scaling arguments of GV to flows with mean shear requires taking note of a third time scale $\tau_S \sim 1/S$, where S is the magnitude of the mean shear, and τ_S is the shear time scale (see table 2 for a summary of our revised scaling relationships). Before proceeding, we impose two restrictions to limit the flows of interest. First, we limit our consideration to flows with vertically sheared, mean horizontal velocities (i.e. turbulence involving $\partial_z\bar{u}$ and $\partial_z\bar{v}$) such that $S^2 = (\partial_z\bar{u})^2 + (\partial_z\bar{v})^2$. Furthermore, we only choose to consider flows with minimal temporal variations of S and N^2. For flows with non-negligible temporal variations of S and N^2 (e.g. Kirkpatrick *et al.* 2019, 2020; Onuki, Joubaud & Dauxois 2021; Issaev *et al.* 2022), we would need to account for two additional time scales associated with $\partial_t S$ and $\partial_t N^2$ for a total of five physical time scales (or four non-dimensional parameters) when estimating Γ using (2.1). In the following discussion, we take the simplest limit of vertically sheared, stably stratified turbulence where $\partial_t N^2 = \partial_t S = 0$, which is true for homogeneous problems where N^2 and S are uniform in space and constant in time.

	$Fr_k = \epsilon_k/(Nk) \sim \tau_B/\tau_L$	$\tau_1\tau_2$	$\Gamma = B/\epsilon_k \sim N^2\tau_1\tau_2$
Sheared, weakly stratified	$Fr_k > 1, \tau_B > \tau_L$	$\tau_L\tau_S$	$\Gamma \sim Fr_k^{-2}S_*^{-1}$
Sheared, moderately stratified	$Fr_k \sim O(1), \tau_B \sim \tau_L$	$\tau_B\tau_S$	$\Gamma \sim Fr_k^{-1}S_*^{-1}$
Sheared, strongly stratified	$Fr_k < 1, \tau_B < \tau_L$	$(\tau_B^3/\tau_L)^{0.5}\tau_S$	$\Gamma \sim Fr_k^{-0.5}S_*^{-1}$

Table 2. Revised scaling for sheared stably stratified turbulence.

For these simplest vertically sheared, stably stratified turbulent flows, we only need to compare the magnitude of τ_S with τ_L and τ_B to decide how the shear time scale should factor into (2.1). To proceed, we can combine the three time scales as

$$S_* = Sk/\epsilon_k \sim \tau_L/\tau_S, \tag{2.2}$$

$$Ri_g = N^2/S^2 \sim (\tau_S/\tau_B)^2\,, \tag{2.3}$$

where S_* is the non-dimensional shear parameter, and Ri_g is the gradient Richardson number. First, we note that $S_* > 1$ is typically observed for unstratified turbulent shear flows (e.g. tables 5.3 and 7.2 of Pope 2000) as well as for stably stratified turbulent shear flows across a wide range of stratification strengths (e.g. Shih *et al.* 2000). Second, we restrict our scaling analysis to a shear-dominant regime where $Ri_g < 1$. Together, these two constraints lead to $\tau_S < \tau_L, \tau_B$, and therefore, we always incorporate τ_S as one of the two time scales in (2.1). For the remaining time scale in (2.1), we choose either τ_L for weakly stratified turbulence or τ_B for moderately stratified turbulence, following the original GV scaling arguments. Here, we have refrained from specifically attributing τ_S to either τ_1 or τ_2 to avoid the ambiguity we highlighted at the end of the previous section. With these choices, we find $\Gamma \sim Fr_k^{-2}S_*^{-1}$ for weakly stratified sheared turbulence, and $\Gamma \sim Fr_k^{-1}S_*^{-1}$ for moderately stratified sheared turbulence. The scaling process, however, is inconclusive for strongly stratified sheared turbulence, so we empirically explore this regime using two DNS datasets of homogeneous, sheared, stably stratified turbulence in § 4 and find $\Gamma \sim Fr_k^{-0.5}S_*^{-1}$. Once again, the GV and revised scaling arguments are summarized in tables 1 and 2, respectively.

Before ending this section, we would like to focus briefly on our assumption that $\partial_t N^2 = \partial_t S = 0$, which in fact technically excludes our revised scaling from applying to stably stratified shear layers. This is an important issue that needs to be addressed given that these flows are considered to be an appropriate model problem for the actual irreversible mixing occurring in Earth's oceans (e.g. Mashayek *et al.* 2017; Salehipour & Peltier 2019; Mashayek, Caulfield & Alford 2021; Mashayek *et al.* 2022). While there has been some success in describing Γ from these flows as a function of Fr (see figure 17 of VanDine, Pham & Sarkar 2021), it appears that Fr alone is insufficient to fully characterize the behaviour of Γ for this class of flows. For example, for forced stably stratified turbulence, Howland, Taylor & Caulfield (2020) showed that Γ could vary by roughly 30 % at the same turbulent Froude number ($Fr \approx 10^{-2}$), indicating that while the power-law exponent in $\Gamma \approx aFr_k^{-\beta}$ can be estimated, the variations of the scaling coefficient a need to be captured by an additional parameter. This type of sensitivity of Γ to the turbulence generation mechanism has also been noted for stably stratified shear layers when contrasting the mixing properties of Kelvin–Helmholtz and Holmboe systems (Salehipour, Caulfield & Peltier 2016). This effect will be further pronounced for buoyancy-driven flows where very efficient mixing is expected (e.g. Davies Wykes, Hughes & Dalziel 2015;

Bou-Zeid *et al.* 2018). Furthermore, as will be shown in § 4, our revised scaling seems to suggest that not only are the transition values of Fr_k distinct between sheared and body-forced stably stratified turbulent flows, but that the power-law exponents predicted by the GV scaling need to be modified when shear is introduced into the system. Going back to the $\Gamma \approx aFr_k^{-\beta}$ formulation, this implies that Fr_k alone is insufficient for estimating the power-law exponent β for sheared, stably stratified turbulence.

Given these points, we expect our revised scaling for sheared, stably stratified turbulence with constant mean shear and stratification to apply more broadly to even describe Γ from stably stratified shear layers. How much our revised scaling needs to be modified to account for time-varying mean shear and stratification will depend on how quickly these two mean quantities evolve relative to the turbulence statistics. If they evolve slowly relative to the turbulence, then very minor (and possibly even no) modifications may be necessary. The fact that the GV scaling is successful at capturing the mixing dynamics of temporally decaying stably stratified turbulence provides further inkling that our revised scaling relationships could apply to a wider range of flows than we have explicitly proposed them for.

3. Shear-forced model problem

3.1. *Equations of motion and solution methodology*

To generate a second database of sheared, stably stratified turbulence, we studied the incompressible, Navier–Stokes equations under the Boussinesq approximation with a linear shear forcing (Dhandapani, Rah & Blanquart 2019)

$$\frac{\partial u_j}{\partial x_j} = 0, \tag{3.1}$$

$$\frac{\partial u_j}{\partial t} + u_m \frac{\partial u_j}{\partial x_m} = -\frac{1}{\rho_0}\frac{\partial p}{\partial x_j} - \frac{g}{\rho_0}\rho\delta_{j3} + \nu\frac{\partial^2 u_j}{\partial x_m \partial x_m} - wS\delta_{j1}, \tag{3.2}$$

$$\frac{\partial \rho}{\partial t} + u_m \frac{\partial \rho}{\partial x_m} + w\frac{\mathrm{d}\bar{\rho}}{\mathrm{d}z} = D\frac{\partial^2 \rho}{\partial x_m \partial x_m}. \tag{3.3}$$

In (3.1)–(3.3), u_j, p, ρ represent velocity, pressure and density fluctuations, respectively, $\bar{\rho}(z)$ is the linearly varying, stable, background density field, g is the gravitational acceleration, ρ_0 is the reference density, ν is the kinematic viscosity of the fluid, D is the molecular diffusivity of density and S is the forcing rate associated with the linear shear forcing. Tensor indices (1, 2, 3) correspond to spatial directions (x, y, z) and velocity fields (u, v, w) with gravity acting along the z-axis.

Unlike classical homogeneous sheared turbulence, this particular system, which we will refer to as the shear-forced model problem, has no mean velocity field, but it does have the same right-hand side forcing term in (3.2) as its classical counterpart, which then leads to the same shear production term in the TKE equation. While (3.1)–(3.3) lead to identical volume-averaged turbulence budgets, there is a modified pre-factor in the Poisson equation for the pressure fluctuations, so the volume-averaged pressure-strain correlations and, consequently, the relative magnitudes of the Reynolds stresses differ from their classical counterparts (see tables 1 and 2 of Dhandapani *et al.* 2019). In § 3.2, we quantitatively compare the turbulence of the shear-forced model problem with that of stably stratified homogeneous shear flow from Shih *et al.* (2005).

We solved (3.1)–(3.3) for triply periodic domains (either cubic with length $L = 2\pi$ or rectangular with $L_x = 4\pi$ and $L_y = L_z = 2\pi$) using our own Fourier pseudospectral

	L_x, L_y, L_z (m)	N_x, N_y, N_z	Δt (s)	ν, κ (m^2 s^{-1})	g (m s^{-2})	ρ_0 (kg m^{-3})
Cubic (C)	$2\pi, 2\pi, 2\pi$	64, 64, 64	2.5×10^{-3}	5×10^{-2}	9.8	1
Rectangular (R)	$4\pi, 2\pi, 2\pi$	128, 64, 64	2.5×10^{-3}	5×10^{-2}	9.8	1

Table 3. Global input parameters for the numerical simulations. Simulations C1–C6 and R16 (see table 4) used $\Delta t = 1.25 \times 10^{-3}$ for numerical stability.

solver with an RK4 time-stepping scheme, where the rectangular domain simulations were conducted to explore domain-size effects. Global and simulation-specific parameters are provided in tables 3 and 4, respectively, where the quantities in columns 3–10 of table 4 are values calculated from volume and time averaging over the statistically stationary portions of each simulation. The fourth-order temporal accuracy and nonlinear advection terms were verified by comparing our numerical solutions with the analytical solutions of a decaying, two-dimensional, Taylor–Green vortex (Canuto *et al.* 2007), and the nonlinear terms were dealiased exactly by zero padding (Canuto *et al.* 2006). Finally, we implicitly verified the linear shear forcing and density coupling by considering the volume-averaged TKE ($k = \overline{u_j u_j}/2$) and turbulent potential energy (TPE) ($k_p = \alpha^2 \overline{\rho\rho}/2$) budgets associated with (3.1)–(3.3)

$$\frac{\mathrm{d}k}{\mathrm{d}t} = -\overline{uw}S - \frac{g}{\rho_0}\overline{w\rho} - \nu\overline{\frac{\partial u_j}{\partial x_m}\frac{\partial u_j}{\partial x_m}} = P_k - B - \epsilon_k, \tag{3.4}$$

$$\frac{\mathrm{d}k_p}{\mathrm{d}t} = \frac{g}{\rho_0}\overline{w\rho} - D\alpha^2\overline{\frac{\partial \rho}{\partial x_m}\frac{\partial \rho}{\partial x_m}} = B - \epsilon_p. \tag{3.5}$$

In (3.4) and (3.5), $\alpha = g/(\rho_0 N)$ is a constant and uniform dimensional factor, which converts the dimensions of density to those of velocity, P_k is the rate of production of TKE from the shear forcing, B is the buoyancy flux and ϵ_k and ϵ_p are the dissipation rates of TKE and TPE, respectively. Subscripts k and p indicate quantities associated with TKE and TPE and do not indicate tensor indices.

In figure 1(*a*,*b*) we plot the steady-state volume- and time-averaged TKE (3.4) and TPE (3.5) budgets as a function of the gradient Richardson number ($Ri_g = N^2/S^2$) with all terms normalized such that they are bounded between ± 1. Filled symbols represent values from the cubic domain simulations, and open symbols represent values from the rectangular domain simulations. For the TKE budget (figure 1*a*), we note that the production term (black triangles) accounts for all of the TKE generation at all values of Ri_g, while the sum of the buoyancy flux and TKE dissipation rate (orange stars and red triangles) account for the total loss of TKE. As Ri_g increases, the buoyancy flux becomes an increasingly significant sink of TKE until $Ri_g = 1/4$, above which its relative magnitude remains unchanged until $Ri_g = 1$ where it diminishes in magnitude. Similar behaviour is noted for the TKE dissipation rate, where it becomes an increasingly less important sink of TKE until $Ri_g = 1/4$, above which its relative magnitude remains unchanged until $Ri_g = 1$ where it increases in magnitude. For the TPE budget (figure 1*b*), we observe that the buoyancy flux accounts for the total generation of TPE (orange stars), and the TPE dissipation rate (red triangles) accounts for the total loss of TPE. For both budgets, the residuals (grey squares) are near zero, indicating that our simulations are exhibiting the expected statistically stationary dynamics described by (3.4) and (3.5).

Sim.	Ri_g	Fr_k	S_*	Re_L	Re_b	Re_S	l_O/L	l_C/L	$\kappa_{max}\eta$
C1	1/1024	13.43	2.38	183.64	37274.87	36.40	22.44	0.12	1.65
C2	1/512	9.48	2.39	186.85	18711.79	36.55	13.37	0.12	1.65
C3	1/256	6.66	2.40	177.25	8722.92	34.07	7.68	0.12	1.68
C4	1/128	4.62	2.45	173.90	4164.84	32.54	4.46	0.12	1.70
C5	1/64	3.21	2.49	175.48	1990.71	31.10	2.59	0.11	1.71
C6	1/32	2.14	2.64	307.28	1540.23	48.13	1.40	0.10	1.12
C7	1/16	1.42	2.81	189.00	418.93	26.18	0.73	0.091	1.55
C8	3/32	1.10	2.97	115.02	154.08	14.44	0.44	0.075	1.99
C9	3/32	1.09	2.98	191.37	262.72	24.63	0.47	0.079	1.41
C10	1/8	0.89	3.18	92.77	83.66	10.46	0.33	0.068	2.33
C11	1/8	0.87	3.24	159.27	134.44	16.81	0.31	0.065	1.55
C12	5/32	0.75	3.39	64.05	39.77	6.21	0.22	0.056	2.79
C13	5/32	0.72	3.52	135.54	76.01	11.88	0.22	0.055	1.68
C14	3/16	0.66	3.48	49.70	24.44	4.58	0.18	0.050	3.15
C15	3/16	0.62	3.70	120.99	49.93	9.36	0.17	0.049	1.78
C16	1/4	0.54	3.72	34.67	11.65	2.91	0.12	0.043	3.81
C17	1/4	0.50	3.99	117.78	32.14	8.03	0.12	0.041	1.70
C18	9/32	0.46	4.10	117.38	26.70	7.51	0.11	0.041	1.78
C19	5/16	0.42	4.23	101.56	20.02	6.26	0.092	0.038	1.91
C20	49/144	0.39	4.35	122.23	21.00	7.15	0.087	0.039	1.75
C21	11/32	0.39	4.36	103.74	17.20	5.91	0.085	0.038	1.98
C22	4/9	0.32	4.72	121.60	13.55	6.02	0.065	0.036	1.83
C23	9/16	0.27	4.91	132.94	11.47	6.45	0.057	0.037	1.81
C24	25/36	0.23	5.31	148.50	8.83	6.13	0.047	0.036	1.85
R1	1/32	2.20	2.57	252.15	1328.70	41.52	1.78	0.13	1.59
R2	1/16	1.47	2.72	241.68	591.55	36.97	1.00	0.12	1.65
R3	3/32	1.15	2.85	266.03	404.39	37.91	0.69	0.12	1.52
R4	1/8	0.94	3.00	239.78	263.91	32.99	0.52	0.11	1.59
R5	5/32	0.79	3.21	252.72	184.76	28.87	0.41	0.10	1.63
R6	3/16	0.68	3.41	261.39	147.58	27.67	0.33	0.094	1.55
R7	1/4	0.54	3.71	242.97	90.89	22.72	0.24	0.085	1.64
R8	9/32	0.48	3.89	251.13	67.81	19.07	0.20	0.078	1.69
R9	5/16	0.46	3.87	264.60	67.68	21.15	0.18	0.077	1.56
R10	11/32	0.44	3.90	279.17	62.88	21.61	0.17	0.078	1.55
R11	4/9	0.36	4.11	275.51	44.00	19.56	0.14	0.074	1.59
R12	9/16	0.32	4.17	351.94	40.49	22.78	0.12	0.076	1.44
R13	25/36	0.26	4.53	454.80	35.28	24.50	0.095	0.072	1.29
R14	121/144	0.18	6.15	546.12	18.76	15.76	0.066	0.058	1.46
R15	17/20	0.20	5.53	538.81	22.43	19.07	0.072	0.063	1.38
	—	0.18	6.05	524.70	19.03	16.18	0.066	0.058	1.46
R16	7/8	0.18	5.99	532.85	17.85	15.62	0.063	0.057	1.44
	—	0.16	6.60	636.29	17.82	15.59	0.063	0.057	1.47
R17	9/10	0.12	8.98	700.77	10.64	9.57	0.495	0.045	1.68
R18	1	0.17	5.84	575.35	18.26	18.26	0.062	0.062	1.40
	—	0.14	6.90	673.25	16.21	16.21	0.059	0.059	1.51
	—	0.082	12.23	958.02	6.54	6.54	0.037	0.037	1.82
	—	0.058	17.12	1250.12	4.37	4.37	0.030	0.030	1.99

Table 4. Non-dimensional input and output parameters of interest for the Yi & Koseff (YK) dataset. For the columns with non-dimensional length scales, L denotes the cubic domain length of 2π, and $l_O = (\epsilon_k/N^3)^{1/2}$, $l_C = (\epsilon_k/S^3)^{1/2}$ and $\eta = (\nu^3/\epsilon_k)^{1/4}$ denote the Ozmidov, Corrsin and Kolmogorov length scales, respectively; $Re_L = k^2/(\nu\epsilon_k)$, $Re_b = \epsilon_k/(\nu N^2)$ and $Re_S = \epsilon_k/(\nu S^2)$ represent the large-eddy, buoyancy and shear Reynolds numbers, respectively. For simulations R15, R16 and R18, time-averaged statistics have been calculated over multiple segments to avoid averaging over times when Re_b was below a turbulence threshold, which we selected to be $Re_b = 1$.

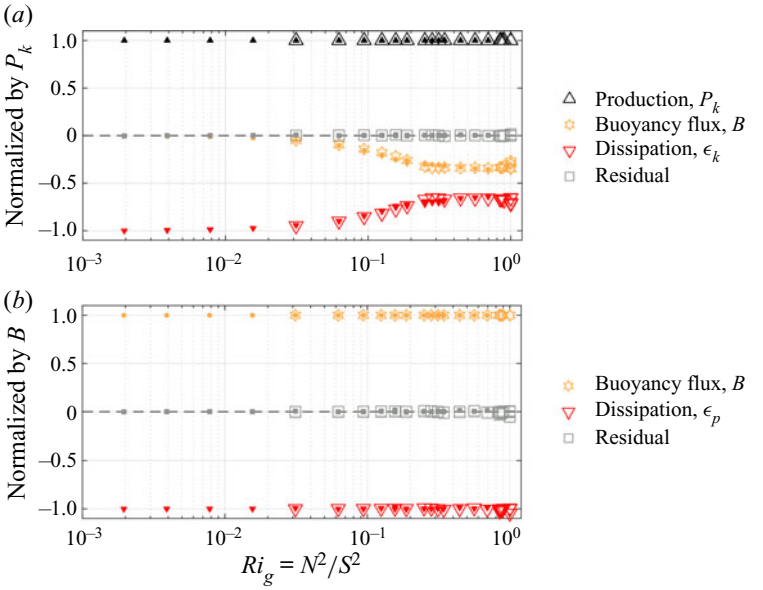

Figure 1. Steady-state volume- and time-averaged budgets of (*a*) TKE and (*b*) TPE as a function of the gradient Richardson number. The two panels correspond to (3.4) and (3.5), respectively. Filled symbols represent values from the cubic domain simulations, and open symbols represent values from the rectangular domain simulations. Given that the residuals of the volume- and time-averaged TKE and TPE budgets are near zero (grey squares in panels *a*,*b*), we take this as a verification that our numerical solver is accurately solving (3.1)–(3.3).

3.2. *Comparison of shear-forced model problem with homogeneous shear flow*

To quantitatively characterize the differences between the stably stratified, homogeneous shear flow considered in Shih *et al.* (2005) (SKIF) and the shear-forced model problem introduced in § 3.1 (YK), we plot b_{13}, S_*, Fr_k as a function of Ri_g for the SKIF and YK datasets with $Re_b = \epsilon_k/(\nu N^2)$ in colour. Here, b_{13} is the $i = 1$, $j = 3$ entry of the normalized Reynolds-stress anisotropy tensor $b_{ij} = \overline{u_i u_j}/(2k) - (1/3)\delta_{ij}$. The horizontal dashed lines in panels (*a*,*b*) indicate typical ranges of b_{13} and S_* that have been observed in experiments and simulations of homogeneous shear flows under neutral conditions (values are from table 2 of Kasbaoui *et al.* 2017), and the dashed-dotted line in panel (*b*) indicates $S_* = 5.5$ (or $Sq^2/\epsilon_k = 11$), which is the late-time, asymptotic value approached by the three DNS runs of Kasbaoui *et al.* (2017). There are some notable differences between the two flows as shown in these plots. First, the SKIF and YK datasets exhibit different values of b_{13} at similar values of Ri_g and Re_b, and the b_{13} values from the YK dataset only begins to fall within the typical range for cases with strong stratification when $Ri_g > 0.3$. For weak stratification ($Ri_g < 0.1$), the SKIF dataset exhibits $b_{13} \approx -0.15$, and the YK dataset exhibits $b_{13} \approx -0.2$. Second, regarding S_*, the SKIF dataset exhibits values between 4 and 6 across a wide range of Ri_g. The YK dataset, however, exhibits $S_* \approx 2$ for $Ri_g < 0.1$, which then also increases monotonically with increasing Ri_g. Finally, the SKIF and YK datasets also exhibit different values of Fr_k at similar values of Ri_g and Re_b, but this difference largely disappears for $Ri_g > 0.2$.

Another way to compare the turbulence characteristics of the SKIF and YK datasets is by considering (3.4) and (3.5) under statistically stationary conditions. Doing so leads to

either of the following relationships:

$$S_* = -\frac{(1+\Gamma)}{2b_{13}}, \quad \frac{N}{S} = -\frac{2b_{13}}{Fr_k\,(1+\Gamma)}, \tag{3.6a,b}$$

which can be related to the growth rate of the TKE (e.g. Holt, Koseff & Ferziger 1992; Jacobitz, Sarkar & Van Atta 1997; Shih *et al.* 2000). In (3.6*a*,*b*), $\Gamma = \epsilon_p/\epsilon_k$ is the irreversible mixing coefficient. The first expression has been considered by Shih *et al.* (2000) for stably stratified, homogeneous shear flow, which broadly exhibits transient growth or decay depending on the sign of the sum of the right-hand side terms in (3.4). Over a narrow range of Reynolds and Richardson numbers, however, the turbulence reaches statistically stationary states (e.g. see figure 10 of Shih *et al.* (2000) and also Portwood, de Bruyn Kops & Caulfield 2019). The second expression is closely related to the first, but it connects N/S, which is prescribed in homogeneous simulations, to output quantities on the right-hand side.

We plot the quantities on the right-hand side of (3.6*a*,*b*) as a function of a scaled version of the non-dimensional shear parameter and the gradient Richardson number in figure 3 for the SKIF and YK datasets. The dashed lines represent $y = 100x$ (black) and $y = x^{1/2}$ (blue), respectively, and the points that lie close to these dashed lines indicate statistically stationary turbulence. For the SKIF dataset, we see that only the simulations with $Ri_g \approx 0.1$ to 0.2 lie close to the dashed lines, which corresponds to the range of stationary Ri_g values observed in Shih *et al.* (2000). Simulations with Ri_g outside of this range, however, deviate from the dashed lines, corresponding to either temporally growing ($Ri_g < 0.1$) or decaying conditions ($Ri_g > 0.2$). In contrast, the YK simulations exhibit statistically stationary behaviour for $Ri_g \approx 10^{-3}$ to 1 indicated by their proximity to the dashed lines. We take this as another verification that our numerical solver is accurately evaluating equations (3.1)–(3.3).

Before testing our revised scaling relationships using the SKIF and YK datasets, we would like to summarize as follows. The stably stratified, homogeneous shear flow of SKIF and the stably stratified, shear-forced model problem studied here exhibit meaningful differences as shown in figures 2 and 3. In particular, they evolve differently in time for a given value of Ri_g due to the presence or absence of advection by the mean flow, which physically shears and elongates the turbulent structures in true shear flows. These effects have important implications for the transition to turbulence (Mashayek & Peltier 2011, 2012*a*,*b*) as well as for the mixing properties of scalars in these flows once turbulence is established (e.g. Salehipour & Peltier 2015). Nonetheless, because the volume-averaged TKE and TPE dynamics of both flows are described by (3.4) and (3.5), the shear-forced model problem provides an additional way to test our revised scaling relationships described in § 2.2. In the next section, we will demonstrate that the power-law scaling relationships connecting Γ, S_*, and Fr_k remain intact for the YK dataset despite these differences and that only the values of the proportionality constants are modified.

4. Results

4.1. *Revised scaling validation using two homogeneous DNS datasets*

We plot the irreversible mixing coefficient $\Gamma = \epsilon_p/\epsilon_k$ as a function of the turbulent Froude number Fr_k in figure 4(*a*) for the SKIF and YK datasets. While the SKIF dataset contains time-varying simulations where $B \neq \epsilon_p$, we still opt to use the irreversible mixing coefficient given its positive semi-definite property compared with the reversible definition B/ϵ_k, which can become negative for large values of Ri_g (see figure 1 of Venayagamoorthy

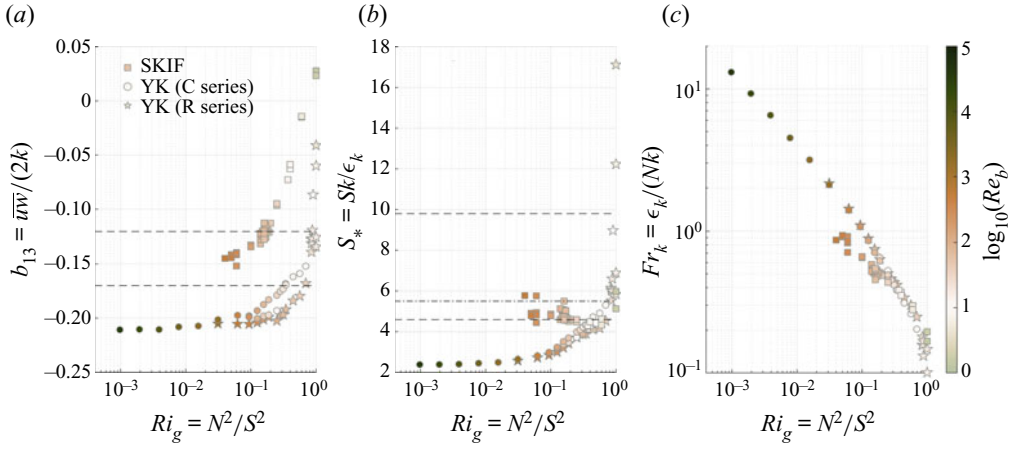

Figure 2. Values of (*a*) b_{13}, (*b*) S_*, (*c*) Fr_k as a function of Ri_g for the SKIF (squares) and YK (circles and stars) datasets with Re_b shown in colour. Time-median values are plotted for the SKIF dataset, and time-averaged values are plotted for the YK dataset. Horizontal dashed lines in panels (*a*,*b*) correspond to typical ranges of b_{13} and S_* found from experiments and DNS of homogeneous shear flows that were reported in table 2 of Kasbaoui *et al.* (2017) (note that there is a factor of 2 difference in what is plotted in panel (*b*) due to $q^2 = 2k$ being typically used to define S_*).

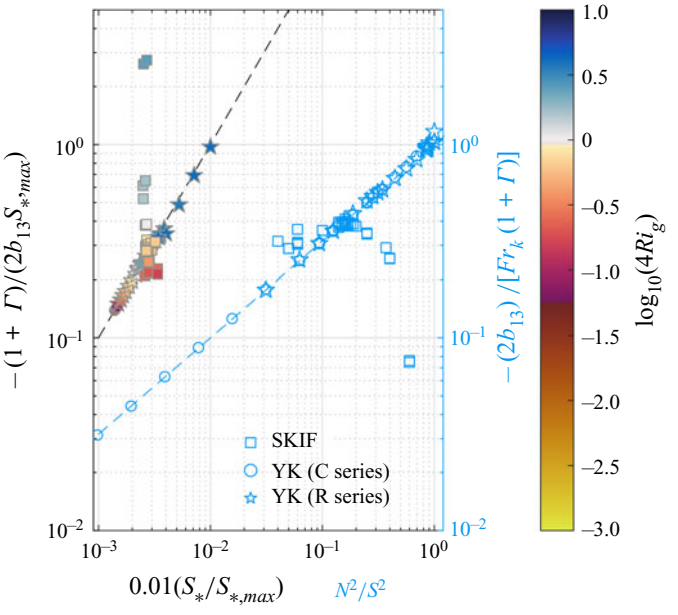

Figure 3. Plot of right-hand side of (3.6*a*,*b*) vs a scaled version of the non-dimensional shear parameter and the gradient Richardson number for the SKIF and YK datasets. The scale of the *x*-axis is the same for both quantities. Here, Ri_g is also shown in colour such that $Ri_g = 1/4$ is shown in light grey. Data that lie along the dashed lines indicate statistically stationary turbulence. The SKIF simulations classified in the paper as stationary ($Ri_g \approx 0.1$ to 0.2) lie close to the dashed lines, but the SKIF simulations that deviate from the dashed lines indicate temporal growth ($Ri_g < 0.1$) or decay ($Ri_g > 0.2$). Most of the YK simulations lie close to the dashed lines.

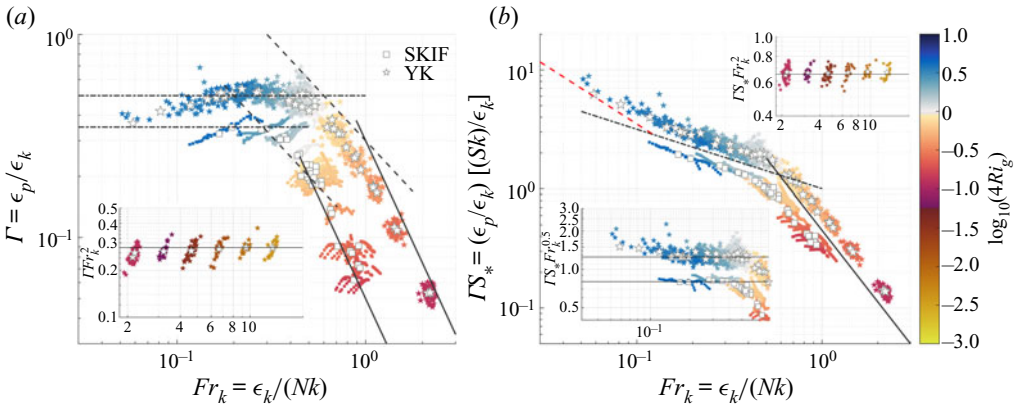

Figure 4. Values of (*a*) Γ and (*b*) ΓS_* as a function of Fr_k for SKIF and YK datasets. Volume-averaged but time-varying quantities are shown in coloured squares (SKIF) and stars (YK) where the colour bar shows Ri_g such that $Ri_g = 1/4$ is shown in light grey. White squares indicate the volume-averaged, time-median values from the SKIF dataset, while the white stars indicate volume- and time-averaged values from the YK dataset. In panel (*a*), the solid, dashed, and dashed-dotted lines mark the $\Gamma \sim Fr_k^{-2}$, Fr_k^{-1} and Fr_k^0 relationships, respectively. In panel (*b*), the solid and dashed-dotted lines mark the $\Gamma S_* \sim Fr_k^{-2}$ and $Fr_k^{-0.5}$ relationships, respectively, and the red dashed line marks $\Gamma S_* \sim Fr_k^{-1}$, which seems to describe the YK dataset for $Fr_k < 0.1$ since $\Gamma \approx 0.4$ and $S_* = 1/Fr_k$ when $Ri_g = 1$. Furthermore, three insets with compensated *y*-axes are included for easier visual comparison with the GV and revised scaling relationships. Only simulations C1–C6 and R1 are shown in the sole inset in panel (*a*) and the top right inset in panel (*b*). The bottom left inset in panel (*b*) tests the scaling relationship for sheared, strongly stratified turbulence.

& Koseff 2016). The small squares (coloured by Ri_g) represent volume-averaged, time-varying values from the SKIF dataset, while the small stars (coloured by Ri_g) represent the volume-averaged, time-varying values from the YK dataset. For the SKIF dataset, the majority of the simulations are either growing or decaying, with only cases with $Ri_g \approx 0.1$ to 0.2 exhibiting statistical stationarity. For the YK dataset, all simulations exhibit statistical stationarity (as demonstrated in figures 1 and 3), and therefore, the time-varying values are only selected from the statistically stationary portions of these simulations. The white squares and stars represent the time-median values from the SKIF dataset and time-mean values from the YK dataset, respectively. From figure 4(*a*), we see that the median and time-averaged values of the SKIF and YK datasets seem to exhibit a $\Gamma \sim Fr_k^{-2}$ behaviour (solid black line) beyond values of $Fr_k \approx 0.6$ and 0.7. This point is further emphasized by the inset showing the results from simulations C1–C6 and R1 of the YK dataset, which shows $\Gamma Fr_k^2 \approx$ const. with small deviations due to the effects of mean shear. For $Fr_k < 0.6$ and $Fr_k < 0.7$, the behaviour seemingly shifts (over a very narrow region) to $\Gamma \sim Fr_k^{-1}$ (dashed black line) before flattening out to values of $\Gamma \approx 0.35$ and 0.5 (dashed-dotted black line) for the SKIF and YK datasets, respectively. We will discuss the YK simulation with $Ri_g = 1$ (blue stars) in a subsequent paragraph.

Next, we test our revised scaling by plotting ΓS_* as a function of Fr_k for the SKIF and YK datasets in figure 4(*b*). We note that the both datasets exhibit $\Gamma S_* \sim Fr_k^{-2}$ (solid black line) for values beyond $Fr_k \approx 0.6$ (SKIF) and 0.7 (YK) in agreement with our revised scaling for weakly stratified sheared turbulence. Notably, we do not observe the moderately stratified sheared turbulence scaling of $\Gamma S_* \sim Fr_k^{-1}$, but both datasets curve over to exhibit $\Gamma S_* \sim Fr_k^{-0.5}$ behaviour (dashed-dotted black line), which is our empirical fit for

the strongly stratified sheared regime. Compared with the GV scaling (figure 4*a*), both the median and time-averaged (white squares and stars) and the time-varying (coloured squares and stars) values exhibit improved collapse under our revised scaling (figure 4*b*). This is especially highlighted by the reduced scatter for $0.4 < Fr_k < 0.7$ for the SKIF dataset under our revised scaling (panel *b*) compared with what is observed under the GV scaling (panel *a*). However, we note that the YK simulation with $Ri_g = 1$ (blue stars) deviates from the empirical scaling of $\Gamma S_* \sim Fr_k^{-0.5}$ for strongly stratified sheared turbulence for $Fr_k < 0.1$ (see the bottom left inset in figure 4*b*). This simulation exhibits $\Gamma \approx 0.4$ for $Fr_k < 0.1$ (figure 4*a*), which is a smaller value than the initial plateau of $\Gamma \approx 0.5$ for $0.2 < Fr_k < 0.5$. A similar behaviour has been observed for the forced (unsheared), stably stratified turbulence simulations of Maffioli *et al.* (2016) and Yi & Koseff (2022) for very strong stable stratifications.

There are two possible interpretations for this behaviour of $\Gamma < \Gamma_{max}$ for decreasing Fr_k. First, we could interpret this as a fourth regime (distinct from the three considered by the GV scaling), similar to that observed for $Fr < 0.3$ in figure 4 from the simulations of Maffioli *et al.* (2016) and $Fr_k < 0.1$ in figure 6(*b*) from the simulations Yi & Koseff (2022). Second, by relaxing our constraint that $Ri_g < 1$ ($\tau_S < \tau_B$) while keeping $S_* > 1$ ($\tau_S < \tau_L$), we can choose $\tau_1\tau_2 \sim \tau_S\tau_B = \tau_B^2$ (since $Ri_g = 1$ for this simulation), which results in $\Gamma \sim Fr_k^0 \approx$ const. when substituted into (2.1). This seems to agree with the behaviour shown in figure 4(*a*) where $\Gamma \approx 0.4$ for $Fr_k < 0.1$ (blue stars). Since $\Gamma \approx 0.4$ for $Fr_k < 0.1$ for the YK simulation with $Ri_g = 1$, we expect the data from this simulation to follow $S_* = 1/Fr_k$, which is shown in figure 4(*b*) using a red dashed line.

Finally, we plot Γ as a function of Re_b in figure 5(*a*) with Ri_g in colour for the SKIF (squares) and YK (circles and stars) datasets. Panels (*b*,*c*) show the same data but with the *y*-axis variable multiplied by $Re_b^{1/2}$ and Re_b, respectively, for easier visual comparison with the expected scaling relationships. Both the SKIF and YK datasets exhibit $\Gamma \sim Re_b^{-1/2}$ ($Re_b > 30$ for SKIF and $30 < Re_b < 500$ for YK) as suggested by Shih *et al.* (2005). The YK dataset, however, also exhibits Re_b^{-1} scaling for $Re_b > 500$, which agrees with $\Gamma \sim Fr_k^{-2}$ (see figure 4*a*) following Maffioli *et al.* (2016) that $Re_b = Re_L Fr_k^2$. Based on our observation that $S_* \approx 2$ for $Ri_g < 0.1$ (figure 2*b*), this behaviour is in agreement with our revised scaling relationship for sheared, weakly stratified turbulence that $\Gamma \sim Fr_k^{-2} S_*^{-1}$. However, S_* still varies for $Ri_g < 0.1$, albeit weakly, and accounting for this variability does lead to an improved characterization of Γ. In particular, simulations C1–C6 and R1 of the YK dataset, corresponding to very weakly stratified conditions, are shown in the bottom left inset of figure 4(*a*) and top right inset of figure 4(*b*). The *y*-axis variable has been compensated by Fr_k^2 and $S_* Fr_k^2$, respectively, so that the time-averaged values of Γ would lie along a flat line if they were well described by the GV or revised scaling relationships. Focusing first on the bottom left inset of figure 4(*a*), the time-averaged values of Γ from simulations C1–C6 and R1 exhibit good agreement with the weakly stratified scaling relationship of GV, but we observe small deviations away from the flat line for simulations corresponding to the larger three Ri_g values. Moving now to the top right inset of figure 4(*b*), the time-averaged values of Γ from simulations C1–C6 and R1 exhibit excellent agreement with our revised weakly stratified scaling relationship, which is shown by the straight line going through all seven white stars. As shown by the large changes in S_* for $Ri_g > 0.1$ in figure 2(*b*), the effects of S_* grow increasingly important with increasing stratification. While the effects of S_* seem less pronounced for weakly stratified conditions, we believe our revised scaling relationships provide an important

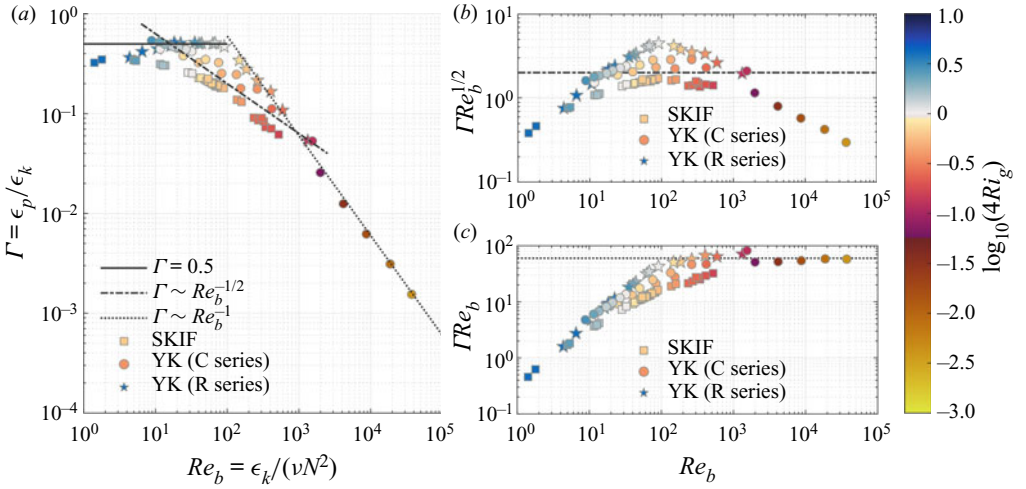

Figure 5. Value of Γ as a function of Re_b with (*a*) no compensation, (*b*) compensation by $Re_b^{1/2}$ and (*c*) compensation by Re_b for the SKIF and YK datasets. The values of Ri_g are shown in colour such that $Ri_g = 1/4$ is shown in light grey.

extension of the GV scaling relationships by explicitly accounting for the effects of mean shear.

4.2. *Applicability testing for more complex sheared, stably stratified turbulent flows*

4.2.1. *Observations*

In this section, we explore the degree of applicability of our revised scaling for the mixing coefficient when some of our simplifying assumptions are relaxed. First, we apply our revised scaling relationships to the DNS dataset of Issaev *et al.* (2022), hereafter IWAN, who considered a spatio-temporally evolving, open channel flow in the presence of radiative heating. This flow is vertically inhomogeneous, and it also has temporally evolving background stratification and shear profiles (i.e. $N^2(z, t)$ and $S(z, t)$). We choose to analyse the IWAN dataset in two ways: (i) using all data for $t > 1$ and $0.2 < z < 0.8$ as in Issaev *et al.* (2022) but keeping only the data with $Re_b > 5$ to exclude the viscosity-affected stratified flow regime (Brethouwer *et al.* 2007); (ii) using all data for $t > 1$ but limiting the vertical range to $0.2 < z < 0.4$ to minimize the effect of vertical transport terms so that the data are well characterized by the simplified TKE balance of $d_t k \approx P_k - B - \epsilon_k$. This allows us to consider the part of the IWAN dataset that corresponds more closely to the homogeneous turbulence dynamics of the SKIF and YK datasets given that enhanced values of the mixing efficiency can be observed even in conditions with weak production but enhanced transport of TKE (e.g. Chamecki, Dias & Freire 2018; Freire *et al.* 2019). We choose a conservative upper limit of $z = 0.4$ based on the statistically stationary profiles of the vertical transport terms of TKE for similar flow configurations as the IWAN dataset that were shown in figure 10(*b*) of Williamson *et al.* (2015). While their figure shows that the transport term decreases in relative importance with larger stability parameters (λ_0) for $0.4 < z < 0.8$, we still apply $z = 0.4$ as the upper limit because in § 5.3 of Issaev *et al.* (2022) we are told that 'all simulations [of the IWAN dataset] are still significantly distant from their final equilibrium states' and that 'the mean shear S is still increasing to obtain shear stress equilibrium such that Ri_g

is still evolving toward its stationary state'. We note that our second analysis approach with subsampled data for $0.2 < z < 0.4$ already satisfies $Re_b > 5$. Finally, because the background stratification profile evolves in time, Issaev *et al.* (2022) opted to use the reversible definition of the mixing coefficient $\Gamma_r = B/\epsilon_k$. Therefore, when applying the GV and our revised scaling relationships to the IWAN dataset, we consider how Γ_r depends on Fr_k and S_*.

We also apply our revised scaling relationships to field measurements of stably stratified atmospheric boundary-layer turbulence that were collected during the MATERHORN program (Fernando *et al.* 2015) and studied by Conry *et al.* (2020) for times when the turbulence dynamics was expected to be well described by the simplified homogeneous TKE and TPE budgets in (3.4) and (3.5) (see Appendix A for more discussion about this assumption). The turbulence is characterized by Taylor microscale Reynolds numbers of $Re_\lambda = \lambda\sqrt{u^2}/\nu \sim O(10^2\text{–}10^3)$ and buoyancy Reynolds numbers of $Re_b = \epsilon_k/(\nu N^2) \sim O(10^3\text{–}10^7)$, where $\lambda = (15\nu u^2/\epsilon_k)^{1/2}$ is the Taylor microscale, and u^2 is the squared streamwise velocity fluctuations. In applying the GV and our revised scaling relationships, we need to account for the fact that the measured variables differ in two ways from those used for the scaling validation with the homogeneous DNS datasets. First, only the streamwise component of the TKE is provided, so we estimate $k \sim u^2$ and define an alternative non-dimensional shear parameter and turbulent Froude number as $S_u = Su^2/\epsilon_k$ and $Fr_u = \epsilon_k/(Nu^2)$. Second, because only the buoyancy flux is provided, we once again consider the reversible mixing coefficient $\Gamma_r = B/\epsilon_k$ and its relationship with Fr_u and S_u.

To characterize these two additional datasets in relation to the previously considered homogeneous DNS datasets, we consider the joint probability density function (p.d.f.) of Fr_k and S_* from the IWAN dataset in figure 6 with the time-median and time-averaged values from the SKIF and YK datasets marked using squares and stars, respectively, along with the measurements from Conry *et al.* (2020) marked using red dots. In figure 6(*a*), all of the IWAN dataset for $t > 1$ and $0.2 < z < 0.8$ with $Re_b > 5$ is used to calculate the joint p.d.f., while in figure 6(*b*), a limited portion of the IWAN dataset for $t > 1$ and $0.2 < z < 0.4$ is used to calculate the joint p.d.f. The dashed and solid diagonal lines indicate $Ri_g = 1/4$ and 1, respectively, for $S_* \geqslant 1$, and the solid horizontal line indicates $S_* = 1$ for $Ri_g \leqslant 1$. The three DNS datasets all exhibit $S_* > 1$, which is one of the limits that were imposed in § 2.2 to arrive at our revised scaling relationships for Γ. The YK dataset broadly exhibits two sets of relationship between S_* and Fr_k: (i) weak relationship between S_* and Fr_k for $Fr_k > 0.3$, and (ii) strong relationship between S_* and Fr_k for $Fr_k < 0.3$. The SKIF dataset exhibits a weak relationship between S_* and Fr_k for its range of Fr_k (0.2 to 1), and S_* remains fairly constant as shown in Shih *et al.* (2000). For $Fr_k > 0.7$, the IWAN dataset exhibits strongly correlated values of S_* and Fr_k but weak rate of change of S_* with respect to Fr_k, corresponding to the weakly stratified regime. For $Fr_k < 0.7$, the IWAN dataset exhibits a strong rate of change of S_* with respect to Fr_k, but the spread in the data suggests a weak correlation between the two quantities, especially for data characterized by $Ri_g > 1/4$ (region between the dashed and solid diagonal lines in figure 6*a*). We note that this weaker correlation for $Ri_g > 1/4$ is associated with the dataset from $0.4 < z < 0.8$ where the mean shear varies temporally and vertical transport terms are expected to be playing an important role. We return to this point regarding additional physical effects in the following paragraphs when exploring the relationships among Γ_r, Fr_k and S_*. Finally, we note that the field measurements studied by Conry *et al.* (2020) exhibit the most variability of Fr_u and S_u with many data points with $Fr_u > 1$ exhibiting $S_u < 1$, which is technically outside the bounds of applicability of our revised scaling, and most of the measurements lie close to the $Ri_g = 1/4$ line.

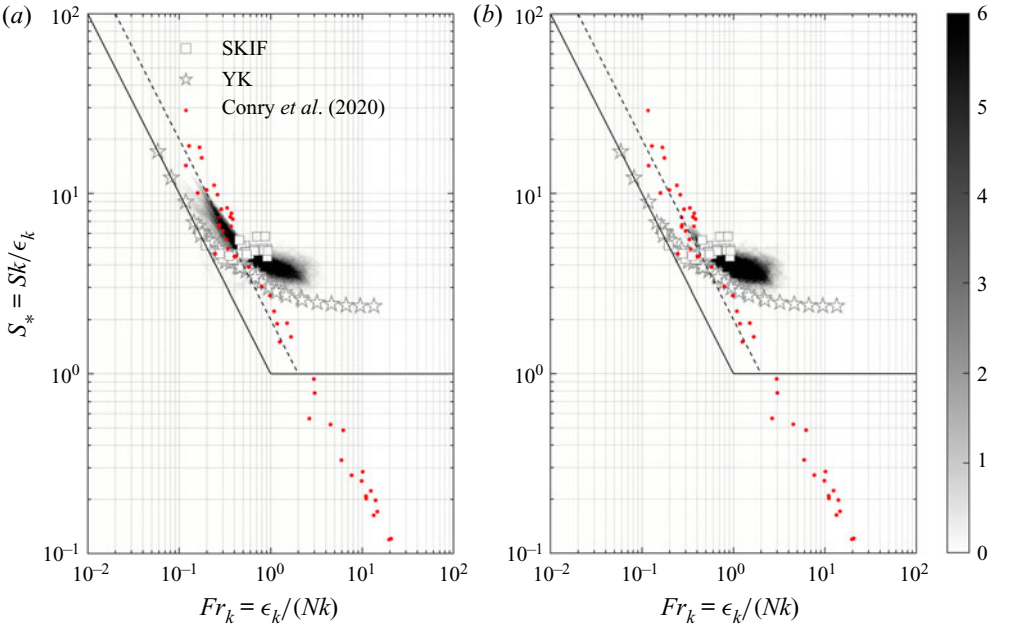

Figure 6. Joint p.d.f. of Fr_k and S_* of the IWAN dataset (light to dark colour bar) with time-median values of SKIF dataset (squares), time-mean values of the YK dataset (stars) and Conry *et al.* (2020) dataset (red dots). The joint p.d.f. in panel (*a*) is calculated using the IWAN dataset for $t > 1$, $0.2 < z < 0.8$, $Re_b > 5$, while the joint p.d.f. in panel (*b*) is calculated using the IWAN dataset for $t > 1$, $0.2 < z < 0.4$. Dark colours denote larger joint p.d.f. values, and the discrete sums over the bins add to unity. Red dots denote the Fr_u and S_u values from Conry *et al.* (2020). The dashed and solid diagonal lines indicate $Ri_g = 1/4$ and 1 for $S_* \geqslant 1$. The solid horizontal line indicates $S_* = 1$ for $Ri_g \leqslant 1$.

In figure 7, we consider the joint p.d.f.s of Fr_k and Γ_r in panels (*a*,*c*) and the joint p.d.f.s of Fr_k and $\Gamma_r S_*$ in panels (*b*,*d*). Panels (*a*,*b*) correspond to the first analysis approach where the IWAN dataset has only been subsampled to satisfy $Re_b > 5$, and panels (*c*,*d*) correspond to the second analysis approach where the IWAN dataset has been subsampled for $0.2 < z < 0.4$ to reduce the effects of time-varying mean shear and vertical transport terms. The GV scaling is revisited in figures 7(*a*) and 7(*c*) using the IWAN dataset, and we observe $\Gamma_r \sim Fr_k^{-2}$ for $Fr_k > 0.7$, $\Gamma_r \sim Fr_k^{-1}$ for $0.3 < Fr_k < 0.7$ and $\Gamma_r \approx 0.3$ for $Fr_k < 0.3$, where this last regime is less visibly obvious due to the subsampling for points satisfying $Re_b > 5$ (see figure 6(*b*) of Issaev *et al.* (2022) for a more visibly obvious demonstration of $\Gamma_r \approx 0.3$ for $Fr_k < 0.3$). Overall, in figures 7(*a*) and 7(*c*), the joint p.d.f.s of the IWAN dataset agree well with the time-median values of the SKIF dataset, and broadly, the three datasets exhibit the same relationships between Γ_r and Fr_k. We note that Issaev *et al.* (2022) used $Fr_k \approx 1$ rather than $Fr_k \approx 0.7$ as their boundary value between the weakly stratified and moderately stratified regimes, and we observe that the subsampled IWAN dataset in figures 7(*c*) and 7(*d*) excludes much of $Fr_k < 0.3$. Next, we consider our revised scaling in figures 7(*b*) and 7(*d*) using the IWAN dataset. First, when considering the entire IWAN dataset for $Re_b > 5$ (figure 7*b*), we observe $\Gamma_r S_* \sim Fr_k^{-2}$ for $Fr_k > 0.7$, but we observe an intermediate scaling of $\Gamma_r S_* \sim Fr_k^{-\alpha}$ with $1 < \alpha < 2$ for $0.3 < Fr_k < 0.7$. For $Fr_k < 0.3$, the IWAN dataset exhibits scatter that lies between $\Gamma_r S_* \sim Fr_k^{-\beta}$ where $0.5 < \beta < 1$, where the smaller power-law slope of -0.5 agrees with the empirical relationship found for strongly stratified sheared turbulence using the

SKIF and YK datasets (see figure 4*b*) and the larger power-law slope of -1 agrees with the moderately stratified sheared turbulence from § 2.2. When we subsample the IWAN dataset for only $0.2 < z < 0.4$, the remaining data points in figure 7(*d*) broadly exhibit $\Gamma_r S_* \sim Fr_k^{-2}$, indicating that the excluded, strongly stratified portions of the IWAN dataset with $Fr_k < 0.3$ exhibit more complicated physics due to unsteady and vertical transport terms that are absent for the SKIF and YK datasets. The SKIF and subsampled IWAN datasets also exhibit good agreement under our revised scaling because the turbulence dynamics for these two flows are very similar for these heights (i.e. well described by (3.4) and (3.5)).

In figure 8(*a*), we plot the reversible mixing coefficient Γ_r as a function of Fr_u using the measurements provided in Conry *et al.* (2020). The data have been colour coded based on the magnitude of S_u (blue for $S_u > 1$ and red for $S_u \leqslant 1$) to distinguish the points that strictly satisfy the requirements for the revised scaling of $S_* \sim S_u > 1$. As described in Conry *et al.* (2020) (and seen in figure 8*a*), these field measurements exhibit $\Gamma_r \sim Fr_u^{-1}$ over most of the Fr_u range (which agrees with the moderately stratified regime of the GV scaling) except for the lowest values of Fr_u (which are possibly beginning to show $\Gamma_r \approx$ const.) and the largest values of Fr_u, where a Fr_u^{-2} fit seems more appropriate. However, when we plot $\Gamma_r S_u$ as a function of Fr_u in figure 8(*b*), we note that the dataset switches to exhibiting $\Gamma_r S_u \sim Fr_u^{-2}$, which is expected for weakly stratified sheared turbulence from our revised scaling. Qualitatively, this shift agrees with the majority of the measurements having been collected during conditions with $Ri_g < 1/4$, and this also broadly agrees with the behaviour of the three DNS datasets for $Ri_g < 1/4$.

4.2.2. *Implications*

We would like to highlight two somewhat unresolved issues based on our observations from figure 7. First, the power-law relationships between ΓS_* and Fr_k for intermediate values of Fr_k (e.g. $0.3 < Fr_k < 0.7$) are different for the homogeneous, sheared, stably stratified turbulence with constant values of N^2 and S (SKIF and YK datasets) compared with the sheared, stably stratified turbulence with time-varying values of N^2 and S (IWAN dataset). For the IWAN dataset, $\partial_t S \neq 0$ and the temporal evolution of the flow seems to be having a significant effect on the local turbulence dynamics. We, therefore, expect that introducing a fourth time scale associated with $\partial_t S$ when considering (2.1) will address a part of this discrepancy. However, the inhomogeneous effects that are present via the vertical transport terms cannot be fully accounted for by this approach. In an attempt to illustrate this point, we isolated the data from the lower heights $0.2 < z < 0.4$ of the IWAN dataset, where the mean shear varies negligibly in time and the vertical transport terms are weak. When we do this, the SKIF and subsampled IWAN datasets agree well, and both datasets exhibit the revised scaling of $\Gamma_r S_* \sim Fr_k^{-2}$ for $Fr_k > 0.7$. Second, we note that the limit of very strong stably stratified turbulence is inaccessible from the IWAN dataset given that most of the dataset for $Re_b > 5$ is characterized by $Fr_k > 0.1$. Therefore, it remains to be seen whether the decrease of Γ from its maximum value and the subsequent plateau for $Fr_k < 0.1$ noted from the YK simulation with $Ri_g = 1$ (see figure 4*a*) would also hold true for other vertically sheared stably stratified turbulent flows.

To resolve the first issue, longer time integration would be necessary until the vertical profiles of S_* became well developed, at which point the dynamically relevant time scales in the IWAN problem would reduce to the same, three, time scales as in the homogeneous, sheared, stably stratified problems explored through the SKIF and YK datasets. Any remaining discrepancy between this statistically steady version of the IWAN dataset and

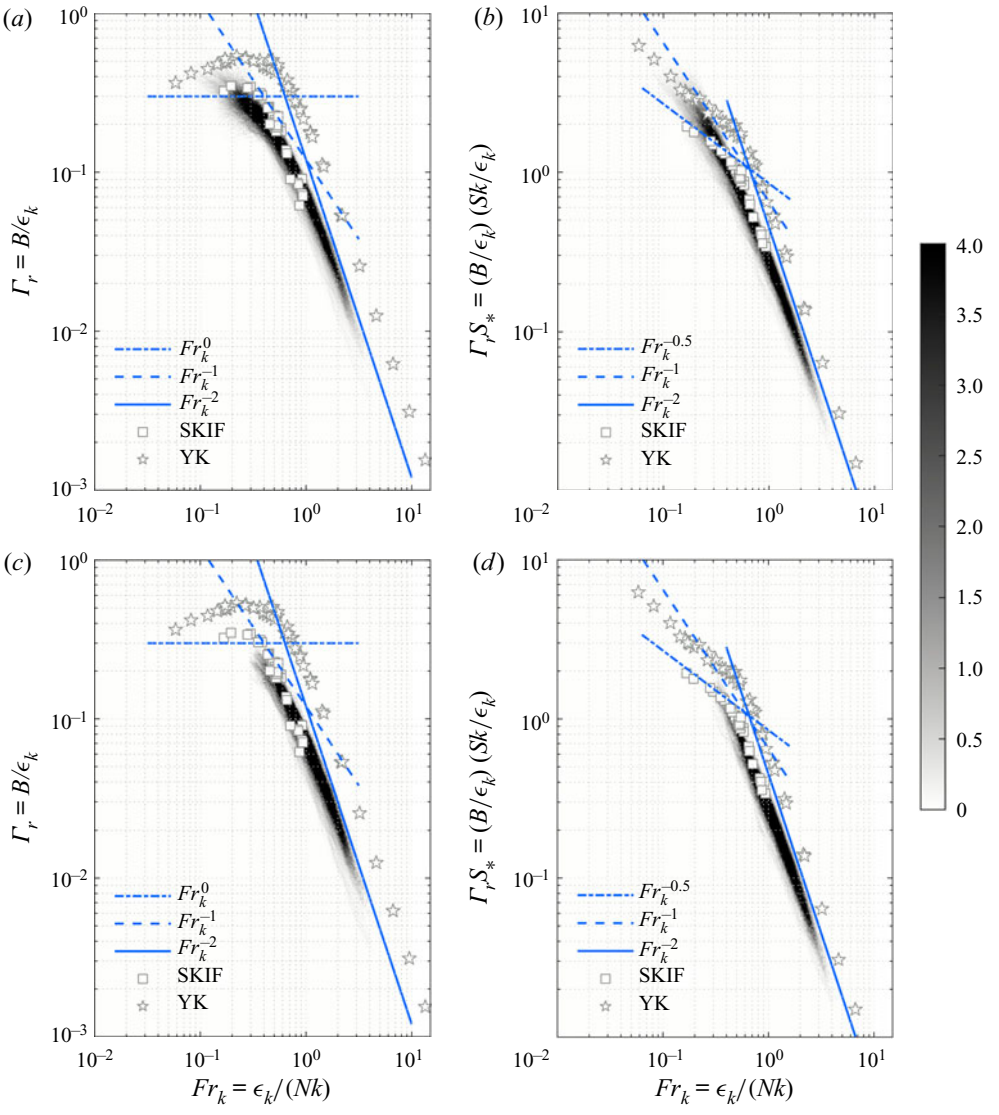

Figure 7. Joint p.d.f.s of Fr_k and (*a*) Γ_r or (*b*) $\Gamma_r S_*$ of the IWAN dataset for $t > 1$, $0.2 < z < 0.8$, and $Re_b > 5$, and joint p.d.f.s of Fr_k and (*c*) Γ_r or (*d*) $\Gamma_r S_*$ of the IWAN dataset for $t > 1$, $0.2 < z < 0.4$. Dark colours denote larger joint p.d.f. values, and the discrete sums over the bins add to unity. White squares and stars indicate the time-median values of the SKIF dataset and time-mean values of the YK dataset, respectively, and the irreversible mixing coefficient values are used ($\Gamma = \epsilon_p/\epsilon_k$). In panels (*a*,*c*), the solid, dashed and dashed-dotted lines mark the $\Gamma \sim Fr_k^{-2}$, Fr_k^{-1} and Fr_k^0 relationships, respectively. In panels (*b*,*d*), the solid, dashed and dashed-dotted lines mark the $\Gamma S_* \sim Fr_k^{-2}$, Fr_k^{-1} and $Fr_k^{-0.5}$ relationships, respectively.

the SKIF and YK datasets could then be unambiguously attributed to vertical transport terms. To resolve the second issue, additional simulations with negligible temporal variations of N^2 and S and with $Ri_g > 1/4$ would need to be explored, which might be challenging given that statistically stationary, sheared, stably stratified turbulence in the presence of walls have typically shown a maximum $Ri_g \approx 0.2$ at heights satisfying energy equilibrium, $P_k \approx B + \epsilon_k$ (e.g. fully developed, radiatively heated, open channel

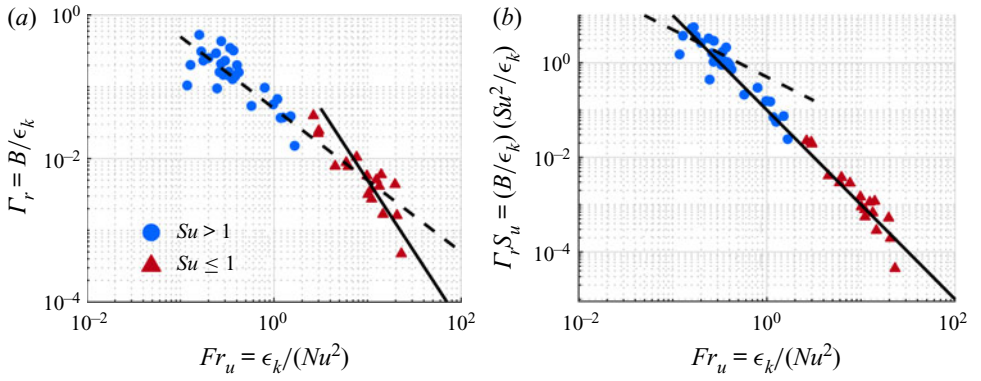

Figure 8. Values of Γ_r and $\Gamma_r S_u$ as a function of Fr_u using the field measurements studied by Conry *et al.* (2020). In panel (*a*), the solid and dashed lines mark the $\Gamma \sim Fr_k^{-2}$ and Fr_k^{-1} relationships, respectively. In panel (*b*), the solid and dashed lines mark the $\Gamma S_* \sim Fr_k^{-2}$ and Fr_k^{-1} relationships, respectively.

flow studied by Williamson *et al.* (2015); fully developed, stably stratified, plane Couette flow studied by Zhou, Taylor & Caulfield 2017).

4.3. *Connections to Ri_g parameterizations of Γ*

Because values of mean shear and stratification are easily measurable and accessible in large-scale modelling contexts, subgrid-scale mixing parameterizations based on Ri_g are regularly used (e.g. Large, McWilliams & Doney 1994; Jackson, Hallberg & Legg 2008; Roekel *et al.* 2018). Therefore, we now examine the connections between our revised scaling and existing ones based on Ri_g. For example, a synthesis of field measurements, laboratory experiments and numerical simulations by Katul *et al.* (2014) shows the mixing efficiency $Ri_f = \Gamma/(1+\Gamma)$ scaling as $Ri_f \sim Ri_g$ for $Ri_g < 1/4$ and $Ri_f \approx$ const. for $Ri_g > 1/4$. Using Monin–Obukhov similarity theory, Zhou *et al.* (2017) showed $Ri_f \sim Ri_g$ and $Fr \sim Ri_g^{-1/2}$, which combined to $Ri_f \sim Fr^{-2}$. They confirmed this scaling using DNS of fully developed, stably stratified, plane Couette flow for varying Reynolds, Richardson and molecular Prandtl numbers. This scaling has also been observed by Kirkpatrick *et al.* (2019) and Issaev *et al.* (2022) using DNS of open-channel flow with temporally evolving thermal stratification.

Using the relationship that $Fr_k = Ri_g^{-1/2} S_*^{-1}$, we can rewrite our revised scaling relationships in table 2 only in terms of Ri_g and S_*. For the weakly stratified sheared regime, this leads to $\Gamma \sim Ri_g S_*$, and for the strongly stratified sheared regime, this leads to $\Gamma \sim Ri_g^{1/4} S_*^{-1/2}$. In figures 2 and 6, we see that S_* weakly varies with Fr_k for weak stratification strengths ($Fr_k > 0.7$) for all three datasets, which explains why all three DNS datasets exhibited $\Gamma \sim Fr_k^{-2}$ and $\Gamma S_* \sim Fr_k^{-2}$ for this range of turbulent Froude numbers, which simplifies to $\Gamma \sim Ri_f \sim Ri_g$. In figures 9(*a*) and 9(*b*), we plot the joint p.d.f. of the gradient Richardson number (Ri_g) and the reversible mixing efficiency ($Ri_{f,r} = B/(\epsilon_k + B)$) for the full but $Re_b > 5$ and subsampled IWAN dataset, respectively. We also plot the median and time-averaged irreversible mixing efficiency ($Ri_f = \epsilon_p/(\epsilon_k + \epsilon_p)$) for the SKIF and YK datasets, respectively, as a function of the gradient Richardson number. In figure 9(*a*), all three datasets exhibit $Ri_f \sim Ri_g$ up to $Ri_g \approx 0.2$ before flattening out. While the time-varying values of Ri_f from the SKIF and YK datasets are not shown, they would lead to vertical lines at each of the Ri_g values of these simulations (see

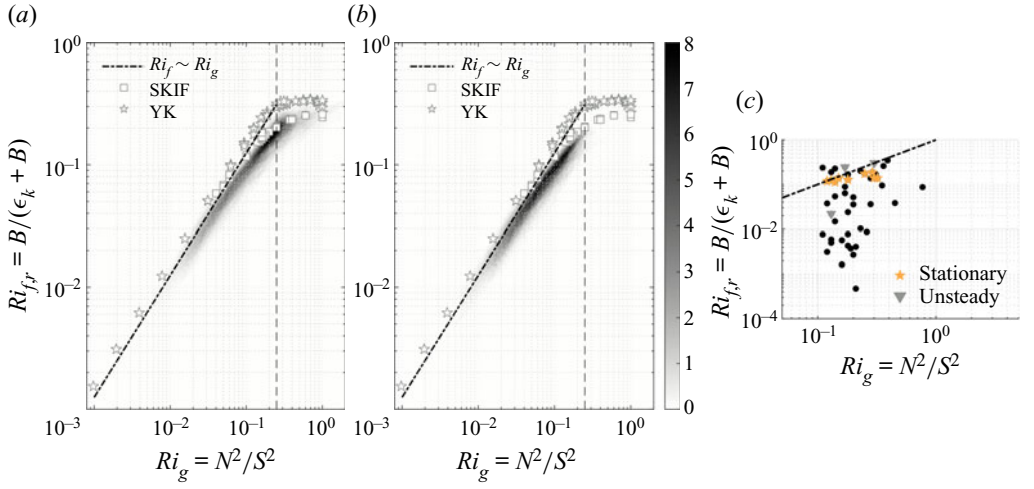

Figure 9. Joint p.d.f. of reversible mixing efficiency ($Ri_{f,r}$) and gradient Richardson number (Ri_g) of the IWAN dataset for (*a*) for $t > 1$, $0.2 < z < 0.8$, and $Re_b > 5$ and (*b*) for $t > 1$, $0.2 < z < 0.4$. Dark colours denote greater joint p.d.f. values, and the discrete sums over the bins add to unity. White squares and stars indicate the time-median values of the SKIF dataset and time-mean values of the YK dataset, respectively, and the irreversible mixing efficiency values are used, $Ri_f = \epsilon_p/(\epsilon_k + \epsilon_p)$. $Ri_{f,r}$ as a function of Ri_g from Conry *et al.* (2020) is plotted in panel (*c*), where a one-to-one line is plotted for reference to indicate $Ri_f \sim Ri_g$.

figure 4 of Venayagamoorthy & Koseff 2016), which remains constant for the entire simulation duration. We further illustrate this shortcoming by plotting $Ri_{f,r}$ as a function of Ri_g in figure 9(*c*) using the field measurements studied by Conry *et al.* (2020). Most of the field measurements do not exhibit the $Ri_f \sim Ri_g$ behaviour for $Ri_g < 0.2$, which strongly suggests that the measurement conditions are described by more complex physics than what is represented by the simplified energetic balance described in (3.4) and (3.5) (see Appendix A for further discussion). While $Ri_f \sim Ri_g$ has been shown to be a good approximation for $Ri_g < 0.2$ by Venayagamoorthy & Koseff (2016) as well as Issaev *et al.* (2022), we note that this relationship begins to break down for moderate and strong stratification strengths ($Fr_k < 0.7, Ri_g > 0.2$), where S_* exhibits stronger variation with Fr_k and Ri_f (or Γ) also exhibits greater variation for a given value of Ri_g (see figure 4 of Venayagamoorthy & Koseff 2016).

4.4. *Finite Reynolds number effects on mixing efficiency*

Up to this point, both the GV and our revised scaling relationships have been presented in terms of Fr_k and S_*. These two quantities primarily describe the effects of large, anisotropic scales of sheared, stratified turbulence, which is in contrast to the various Reynolds numbers that can be introduced for these flows (e.g. large-eddy, buoyancy and shear Reynolds numbers; Re_L, Re_b and Re_S, respectively), which incorporate the effects of isotropic scales (see § 2.2 of Zhang *et al.* (2022) for a further overview and discussion about the energetics associated with the various ranges of scales in sheared, stably stratified flows). The primary variations of Γ seem to be well captured by Fr_k and S_* based on our validation using the SKIF and YK datasets (figure 4) as well as by the IWAN dataset (figure 7) and the data studied by Conry *et al.* (2020) (figure 8). Nevertheless, we expect Γ to exhibit some sensitivity to the Reynolds number.

For forced (unsheared), stably stratified turbulence, Maffioli *et al.* (2016) showed that Γ decreases with increasing Taylor microscale Reynolds number ($Re_\lambda \sim Re_L^{1/2}$) for weakly stratified conditions ($Fr_k \approx 3$). This sensitivity, however, was weak compared with the large variations of Γ that were observed by varying the turbulent Froude number at a fixed Reynolds number. For sheared, stably stratified turbulence under moderately stratified conditions ($0.42 \lesssim Fr_k \lesssim 0.52$), Portwood *et al.* (2019) also showed that Γ decreases with Re_b, albeit very weakly. As Re_b is increased, the dissipation scales become increasingly isotropic, but this effect seems weakly tied to the actual value of Γ (see figures 1 and 2 of Portwood *et al.* 2019).

To explain this weak relationship between Γ and the Reynolds number, which we take to be an estimate of the range of isotropic scales, we consider an alternative expression for the irreversible mixing efficiency ($Ri_f = \epsilon_p/(\epsilon_k + \epsilon_p)$) from Bou-Zeid *et al.* (2018)

$$Ri_f = \frac{1}{1 - c_3}\left(\frac{R_w}{P_k} - c_3\right), \tag{4.1}$$

where $c_3 = \epsilon_w/\epsilon_k$ is the fraction of the TKE dissipation rate that is accounted for by the dissipation rate of the vertical component of TKE ($k_w = \overline{ww}/2$), R_w is the pressure-strain correlation term in the k_w budget, and $P_k = -\overline{uw}S$ is the rate of production of TKE. For large Reynolds numbers, $c_3 \to 1/3$ as expected by the dissipation scales recovering local isotropy (e.g. Itsweire *et al.* 1993; Portwood *et al.* 2019), and (4.1) can be simplified to

$$\lim_{Re \gg 1} Ri_f = \frac{3}{2}\left(\frac{R_w}{P_k} - \frac{1}{3}\right). \tag{4.2}$$

Equation (4.2) connects the irreversible mixing efficiency of homogeneous, sheared, stably stratified turbulence to the normalized pressure-strain correlation (R_w/P_k), which is a large-scale quantity that is expected to primarily depend on Fr_k and S_* rather than on the Reynolds number.

To explore this further, we plot R_w/P_k and c_3 as a function of Fr_k with Re_S shown in colour in figure 10(*a*,*b*). Here we have chosen Re_S to represent the range of isotropic scales because for $Ri_g < 1$, the Corrsin scale (l_C) is smaller than the Ozmidov scale (l_O), making it a more appropriate estimate of the largest isotropic eddies for sheared, stably stratified flows when $Ri_g < 1$. In panel (*a*), the horizontal dashed line indicates the maximum value of $c_3 \approx 0.31$. Given that R_w/P_k is close to this value for $Fr_k \gg 1$, this matches our intuition that $Ri_f \to 0$ for $Fr_k \gg 1$ where there is no background scalar gradient to mix. As Fr_k is decreased, R_w/P_k increases until reaching a maximum at $Fr_k \approx 0.2$ for the C series simulations (circles) and reaching a plateau for $0.2 < Fr_k < 0.6$ for the R series simulations (stars). For $Fr_k < 0.2$, however, R_w/P_k decreases with increasing stratification. In panel (*b*), the horizontal dashed line marks $1/3$, which is the value of c_3 that is expected for isotropic dissipation scales. The value of c_3 generally decreases with increasing stratification (this is because Re_S decreases as stratification is increased due to the fixed resolution of our simulations), but for $0.2 < Fr_k < 1$, we see that c_3 grows with increasing Re_S, as seen by the change from purple to blue coloured symbols with increasing values of c_3. In panel (*c*), $(R_w/P_k - c_3)$ is plotted as a function of Fr_k with Re_S shown in colour. Focusing on $0.2 < Fr_k < 0.7$, where we observe large differences of R_w/P_k and c_3 between the C and R series simulations due to changes in Re_S, we find that the difference, $(R_w/P_k) - c_3$, does not seem as sensitive to Re_S because the simultaneous changes to R_w/P_k and c_3 seem to cancel out. Finally, in figure 10(*d*), we plot the two sides of (4.1) with Fr_k shown in colour to check whether the YK dataset obeys

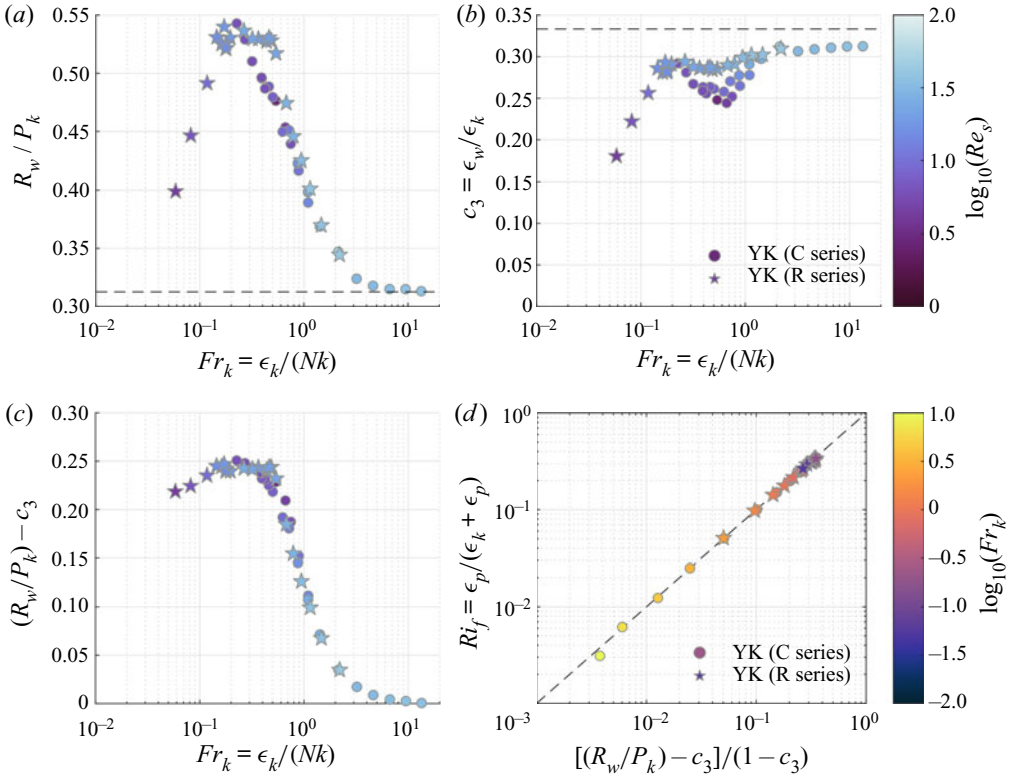

Figure 10. Value of (*a*) R_w/P_k, (*b*) c_3, (*c*) $(R_w/P_k) - c_3$ as a function of Fr_k with Re_S shown in colour. The horizontal dashed line in panel (*a*) indicates the maximum value of $c_3 \approx 0.31$, and the horizontal dashed line in panel (*b*) marks $c_3 = 1/3$, which is expected under conditions of local isotropy of dissipative scales. (*d*) Value of Ri_f as a function of the right-hand side expression of (4.1) with Fr_k in colour. The values from the YK dataset lie along the one-to-one line.

this relationship, which we confirm based on the observation that the data lie along the one-to-one line.

Lastly, (4.1) allows us to explore why the YK dataset exhibits larger values of Γ (or Ri_f) relative to the SKIF dataset as observed in figures 4 and 9. For a given rate of TKE production and Reynolds number, the sheared flow that is associated with larger values of R_w will be more efficient at irreversibly mixing out the background scalar gradient. For homogeneous sheared turbulence, the vertical component of TKE (k_w) is the smallest (e.g. Kasbaoui *et al.* 2017), which is further decreased by the effects of stable stratification as Fr_k is decreased. For the shear-forced model problem, however, k_w is actually the second largest component across all Fr_k values (not shown), which suggests that this model problem involves larger values of R_w/P_k compared with homogeneous sheared turbulence. Also, the volume-averaged vertical buoyancy flux budget has a source term that is linearly proportional to k_w (e.g. Riley, Metcalfe & Weissman 1981; Yi & Koseff 2022). Connecting these two thoughts, our hypothesis is that for a given rate of TKE production and stratification, the shear-forced model problem is associated with larger values of R_w/P_k compared with homogeneous shear turbulence, leading to enhanced values of k_w/k, which can then generate larger vertical buoyancy fluxes. Under a steady-state balance, this implies a larger ϵ_p for a given P_k, and therefore a larger value of Ri_f. In closing this section, we stress that while R_w/P_k in (4.1) seems to depend more sensitively on Fr_k, it

does exhibit some relationship with Re_S. This observation should be looked at in more detail in the future.

5. Conclusions

We revisited the mixing coefficient scaling of Garanaik & Venayagamoorthy (2019) and modified them to include the effects of mean shear for vertically sheared, stably stratified turbulent flows. Through scaling analysis, we found $\Gamma \sim Fr_k^{-2} S_*^{-1}$ for the weakly stratified sheared regime and $\Gamma \sim Fr_k^{-1} S_*^{-1}$ for the moderately stratified sheared regime. While the scaling analysis was inconclusive for the strongly stratified sheared regime, we empirically observed $\Gamma \sim Fr_k^{-0.5} S_*^{-1}$ using two distinct DNS datasets of homogeneous, stably stratified, sheared turbulence as well as the absence of the moderately stratified sheared regime. We then explored the degree of applicability of our revised scaling by considering two datasets of more complex, sheared, stably stratified turbulence. The first dataset was from the spatio-temporally varying, radiatively heated, open channel simulations of Issaev *et al.* (2022), and the second dataset was from field measurements from the MATERHORN campaign that were provided in Conry *et al.* (2020). The dataset of Issaev *et al.* (2022) also exhibited $\Gamma_r S_* \sim Fr_k^{-2}$ for $Fr_k > 0.7$, but it neither exhibited the moderately stratified sheared scaling of $\Gamma S_* \sim Fr_k^{-1}$ nor the empirical strongly stratified sheared scaling of $\Gamma_r S_* \sim Fr_k^{-0.5}$ for $Fr_k < 0.7$, which we hypothesized are due to the effects of the vertical transport terms and time-varying mean shear that were unaccounted for when arriving at our revised scaling relationships. We attempted to explore this hypothesis by minimizing these two additional physical effects by only considering data from the zone where vertical transport was minimal in their simulations ($0.2 < z < 0.4$), which resulted in mostly retaining the data exhibiting $\Gamma_r S_* \sim Fr_k^{-2}$ behaviour (for $Fr_k > 0.7$), which is in good agreement with the SKIF dataset. When we applied our revised scaling to the field measurements analysed by Conry *et al.* (2020), the measurements followed the weakly stratified sheared scaling of $\Gamma_r S_u \sim Fr_u^{-2}$, which was expected given that most measurement conditions were characterized by $Ri_g < 1/4$. Finally, we explored the connection between our revised scaling and existing Ri_g descriptions, and showed that $Ri_f \sim Ri_g$ for $0 < Ri_g < 0.2$ and $Ri_f \approx$ const. for $Ri_g > 0.2$. However, we noted that Ri_g parameterizations remain inadequate for describing temporally varying datasets unlike our revised scaling relationships which include some information about temporal variations through Fr_k and S_*. Lastly, we noted that values of Γ from a simulation with $Ri_g = 1$ deviated from the empirical scaling for strongly stratified, sheared turbulence of $\Gamma S_* \sim Fr_k^{-0.5}$ and instead exhibited $\Gamma \approx$ const. $< \Gamma_{max}$ for $Fr_k < 0.1$, for which we proposed two possible explanations.

In closing, we emphasize that our revised scaling relationships should also hold for other types of stably stratified turbulence with vertically sheared horizontal mean flows satisfying the simplified TKE balance of $d_t k \approx P_k - B - \epsilon_k$, but we have neglected the effects of Prandtl number (e.g. Salehipour, Peltier & Mashayek 2015; Schaad & Venayagamoorthy 2017; Legaspi & Waite 2020) and the Reynolds number (briefly explored in § 4.4), which should be incorporated into (2.1) for a more complete description of irreversible mixing in sheared, stably stratified turbulent flows. Nevertheless, since our revised scaling relationships successfully describe the temporally evolving mixing statistics from Shih *et al.* (2005), we hypothesize that they might also apply to irreversible mixing occurring in stably stratified shear layers (Mashayek & Peltier 2011; Salehipour

& Peltier 2015), especially when the mean shear and stratification evolve slowly relative to the turbulence statistics. Furthermore, relying on the connections between our revised scaling and Re_b-based descriptions that we explored in § 4, there is further hope for the applicability of these relations to stably stratified mixing layers whose mixing properties have been previously studied in terms of Re_b (e.g. Salehipour & Peltier 2015; Mashayek *et al.* 2017; VanDine *et al.* 2021). However, given the challenges associated with accurate measurements of turbulence quantities such as k and ϵ_k that are needed to estimate Fr_k and S_*, it would be beneficial to develop a corresponding length-scale-based characterization of the mixing coefficient as done by Garanaik & Venayagamoorthy (2019) for forced (unsheared), stably stratified turbulence. To do this, we could leverage the large body of work on sheared, stably stratified flows that includes studies of the temporal evolution of various length scales (e.g. Itsweire *et al.* 1993; Smyth & Moum 2000; Smyth, Moum & Caldwell 2001; Lewin & Caulfield 2021) as well as of the relationships between length-scale ratios and the degree of irreversible mixing of these flows (e.g. Ivey & Imberger 1991; Mater & Venayagamoorthy 2014*b*; Ivey, Bluteau & Jones 2018; Ijichi & Hibiya 2018; Mashayek *et al.* 2021, 2022). Lastly, when considering stably stratified turbulence with different shear configurations such as spanwise shear (e.g. Billant & Chomaz 2000*a*,*b*; Basak & Sarkar 2006; Deloncle, Chomaz & Billant 2007; Waite & Smolarkiewicz 2008; Lucas, Caulfield & Kerswell 2017; Cope, Garaud & Caulfield 2020) or flows with spatio-temporal variations (e.g. Williamson *et al.* 2015; Kirkpatrick *et al.* 2019, 2020; Onuki *et al.* 2021; Issaev *et al.* 2022; Lewin & Caulfield 2022), we expect the need for an expanded set of scaling relationships due to the differences in the turbulence generation mechanism or large-scale forcing (Howland *et al.* 2020) and the energy exchange pathways among the different components of TKE and TPE (Yi & Koseff 2022).

Acknowledgements. Y.R.Y. gratefully acknowledges support from the Charles H. Leavell Fellowship of the Department of Civil and Environmental Engineering at Stanford University. Some of the computing for this project was performed on the Sherlock cluster. We would like to thank Stanford University and the Stanford Research Computing Center for providing computational resources and support that contributed to these research results. The authors also greatly thank V. Issaev for sharing the DNS dataset that was analysed in Issaev *et al.* (2022).

Declaration of interests. The authors report no conflict of interest.

Author ORCIDs.
Young R. Yi https://orcid.org/0000-0002-5563-1040;
Jeffrey R. Koseff https://orcid.org/0000-0003-2121-4844.

Appendix A. Steps taken to analyse the Conry *et al.* (2020) dataset

Here, we seek to estimate the degree of statistical stationarity of the measurements that were analysed by Conry *et al.* (2020). For a vertically sheared, stably stratified turbulent flow under statistically stationary and homogeneous conditions, TKE and TPE budgets are described by the balance of right-hand side terms in (3.4) and (3.5). Under these conditions, we can consider three different estimates of the mixing efficiency (Ri_f) and

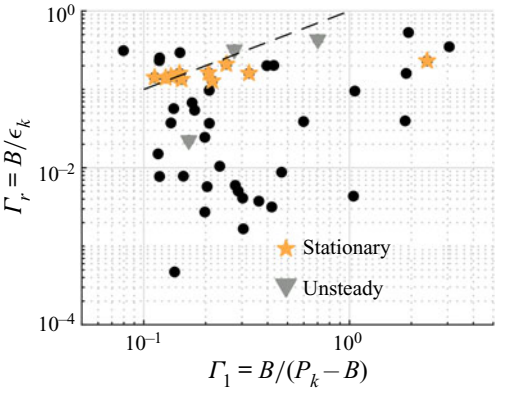

Figure 11. Comparison plot of the two definitions of Γ evaluated using (A1*b*) and (A2*b*) from measurements analysed by Conry *et al.* (2020). Orange stars represent data from statistically stationary conditions, and grey downward-facing triangles represent data from unsteady conditions as labelled by Conry *et al.* (2020). Black circles represent all other measurements. Most of the data points do not lie on the one-to-one line (dashed line), which we interpret as the consequence of more complex physics than what is captured in (3.4) and (3.5) as well as assumptions that were invoked to estimate P_k, B, and ϵ_k.

the mixing coefficient ($\Gamma = Ri_f/(1 - Ri_f)$)

$$Ri_{f,1} = \frac{B}{P_k}, \quad \Gamma_1 = \frac{B}{P_k - B}, \tag{A1a,b}$$

$$Ri_{f,r} = \frac{B}{B + \epsilon_k}, \quad \Gamma_r = \frac{B}{\epsilon_k}, \tag{A2a,b}$$

$$Ri_f = \frac{\epsilon_p}{\epsilon_p + \epsilon_k}, \quad \Gamma = \frac{\epsilon_p}{\epsilon_k}, \tag{A3a,b}$$

where the three definitions correspond to R_f, R_f^{II}, R_f^* from Venayagamoorthy & Koseff (2016). The second set of definitions (A2) can be reached from (A1) by substituting in for P_k using (3.4). The third set of definitions (A3) can be reached from (A2) by substituting in for B using (3.5).

While (A3*a*) robustly estimates the efficiency of the irreversible mixing of the background, vertically varying, stratifying scalar field, there are no measurements of ϵ_p in Conry *et al.* (2020), so we can only consider the first two sets of definitions. Taking the entries from their table 1 with $\Gamma > 0$, we evaluate Γ_1 and Γ_r and plot them in figure 11. The measurements described by Conry *et al.* (2020) to be in statistical stationary conditions are labelled using orange stars, and the measurements described to exhibit unsteady effects are labelled using grey triangles. The remaining measurements are shown using black circles. We note that most of the measurements do not lie on the dashed one-to-one line, which we interpret to be due to assumptions that were invoked to estimate the right-hand side quantities in (3.4) and (3.5), but more importantly due to the flow conditions not being statistically stationary and homogeneous. Conry *et al.* (2020) used Γ_r in their work, and we have also chosen to use this definition in our work given that it is more directly related to the Osborn eddy diffusivity model for the buoyancy flux $D_T \approx B/N^2 \approx \Gamma_r \epsilon_k/N^2$ (Osborn 1980).

References

Basak, S. & Sarkar, S. 2006 Dynamics of a stratified shear layer with horizontal shear. *J. Fluid Mech.* **568**, 19–54.

Billant, P. & Chomaz, J.-M. 2000*a* Experimental evidence for a new instability of a vertical columnar vortex pair in a strongly stratified fluid. *J. Fluid Mech.* **418**, 167–188.

Billant, P. & Chomaz, J.-M. 2000*b* Theoretical analysis of the zigzag instability of a vertical columnar vortex pair in a strongly stratified fluid. *J. Fluid Mech.* **419**, 29–63.

Bou-Zeid, E., Gao, X., Ansorge, C. & Katul, G.G. 2018 On the role of return to isotropy in wall-bounded turbulent flows with buoyancy. *J. Fluid Mech.* **856**, 61–78.

Brethouwer, G., Billant, P., Lindborg, E. & Chomaz, J.-M. 2007 Scaling analysis and simulation of strongly stratified turbulent flows. *J. Fluid Mech.* **585**, 343–368.

Bryan, F. 1987 Parameter sensitivity of primitive equation ocean general circulation models. *J. Phys. Oceanogr.* **17** (7), 970–985.

Canuto, C., Hussaini, M.Y., Quarteroni, A. & Zang, T.A. 2006 *Spectral Methods: Fundamentals in Single Domains*. Springer.

Canuto, C., Quarteroni, A., Hussaini, M.Y. & Zang, T.A. 2007 *Spectral Methods: Evolution to Complex Geometries and Applications to Fluid Dynamics*. Springer.

Caulfield, C.P. 2020 Open questions in turbulent stratified mixing: do we even know what we do not know? *Phys. Rev. Fluids* **5** (11), 110518.

Caulfield, C.P. 2021 Layering, instabilities, and mixing in turbulent stratified flows. *Annu. Rev. Fluid Mech.* **53** (1), 113–145.

Chamecki, M., Dias, N.L. & Freire, L.S. 2018 A TKE-based framework for studying disturbed atmospheric surface layer flows and application to vertical velocity variance over canopies. *Geophys. Res. Lett.* **45** (13), 6734–6740.

Cimoli, L., Caulfield, C.P., Johnson, H.L., Marshall, D.P., Mashayek, A., Naveira Garabato, A.C. & Vic, C. 2019 Sensitivity of deep ocean mixing to local internal tide breaking and mixing efficiency. *Geophys. Res. Lett.* **46** (24), 14622–14633.

Conry, P., Kit, E. & Fernando, H.J.S. 2020 Measurements of mixing parameters in atmospheric stably stratified parallel shear flow. *Environ. Fluid Mech.* **20** (5), 1177–1197.

Cope, L., Garaud, P. & Caulfield, C.P. 2020 The dynamics of stratified horizontal shear flows at low Péclet number. *J. Fluid Mech.* **903**, A1.

Davies Wykes, M.S., Hughes, G.O. & Dalziel, S.B. 2015 On the meaning of mixing efficiency for buoyancy-driven mixing in stratified turbulent flows. *J. Fluid Mech.* **781**, 261–275.

Deloncle, A., Chomaz, J.-M. & Billant, P. 2007 Three-dimensional stability of a horizontally sheared flow in a stably stratified fluid. *J. Fluid Mech.* **570**, 297–305.

Dhandapani, C., Rah, K.J. & Blanquart, G. 2019 Effective forcing for direct numerical simulations of the shear layer of turbulent free shear flows. *Phys. Rev. Fluids* **4** (8), 084606.

Fernando, H.J.S., *et al.* 2015 The MATERHORN: unraveling the intricacies of mountain weather. *Bull. Am. Meteorol. Soc.* **96** (11), 1945–1967.

Fox-Kemper, B., *et al.* 2019 Challenges and prospects in ocean circulation models. *Front. Mar. Sci.* **6**, 65.

Freire, L.S., Chamecki, M., Bou-Zeid, E. & Dias, N.L. 2019 Critical flux Richardson number for Kolmogorov turbulence enabled by TKE transport. *Q. J. R. Meteorol. Soc.* **145** (721), 1551–1558.

Garanaik, A. & Venayagamoorthy, S.K. 2018 Assessment of small-scale anisotropy in stably stratified turbulent flows using direct numerical simulations. *Phys. Fluids* **30** (12), 126602.

Garanaik, A. & Venayagamoorthy, S.K. 2019 On the inference of the state of turbulence and mixing efficiency in stably stratified flows. *J. Fluid Mech.* **867**, 323–333.

Gregg, M.C., D'Asaro, E.A., Riley, J.J. & Kunze, E. 2018 Mixing efficiency in the ocean. *Annu. Rev. Mar. Sci.* **10** (1), 443–473.

Holt, S.E., Koseff, J.R. & Ferziger, J.H. 1992 A numerical study of the evolution and structure of homogeneous stably stratified sheared turbulence. *J. Fluid Mech.* **237**, 499–539.

Howland, C.J., Taylor, J.R. & Caulfield, C.P. 2020 Mixing in forced stratified turbulence and its dependence on large-scale forcing. *J. Fluid Mech.* **898**, A7.

Ijichi, T. & Hibiya, T. 2018 Observed variations in turbulent mixing efficiency in the deep ocean. *J. Phys. Oceanogr.* **48** (8), 1815–1830.

Issaev, V., Williamson, N., Armfield, S.W. & Norris, S.E. 2022 Parameterization of mixing in stratified open channel flow. *J. Fluid Mech.* **935**, A17.

Itsweire, E.C., Koseff, J.R., Briggs, D.A. & Ferziger, J.H. 1993 Turbulence in stratified shear flows: implications for interpreting shear-induced mixing in the ocean. *J. Phys. Oceanogr.* **23** (7), 1508–1522.

IVEY, G.N., BLUTEAU, C.E. & JONES, N.L. 2018 Quantifying diapycnal mixing in an energetic ocean. *J. Geophys. Res.* **123** (1), 346–357.

IVEY, G.N. & IMBERGER, J. 1991 On the nature of turbulence in a stratified fluid. Part I: the energetics of mixing. *J. Phys. Oceanogr.* **21** (5), 650–658.

IVEY, G.N., WINTERS, K.B. & KOSEFF, J.R. 2008 Density stratification, turbulence, but how much mixing? *Annu. Rev. Fluid Mech.* **40** (1), 169–184.

JACKSON, L., HALLBERG, R. & LEGG, S. 2008 A parameterization of shear-driven turbulence for ocean climate models. *J. Phys. Oceanogr.* **38** (5), 1033–1053.

JACOBITZ, F.G., SARKAR, S. & VAN ATTA, C.W. 1997 Direct numerical simulations of the turbulence evolution in a uniformly sheared and stably stratified flow. *J. Fluid Mech.* **342**, 231–261.

JAYNE, S.R. 2009 The impact of abyssal mixing parameterizations in an ocean general circulation model. *J. Phys. Oceanogr.* **39** (7), 1756–1775.

KASBAOUI, M.H., PATEL, R.G., KOCH, D.L. & DESJARDINS, O. 2017 An algorithm for solving the Navier–Stokes equations with shear-periodic boundary conditions and its application to homogeneously sheared turbulence. *J. Fluid Mech.* **833**, 687–716.

KATUL, G.G., PORPORATO, A., SHAH, S. & BOU-ZEID, E. 2014 Two phenomenological constants explain similarity laws in stably stratified turbulence. *Phys. Rev.* E **89** (2), 023007.

KIRKPATRICK, M.P., WILLIAMSON, N., ARMFIELD, S.W. & ZECEVIC, V. 2019 Evolution of thermally stratified turbulent open channel flow after removal of the heat source. *J. Fluid Mech.* **876**, 356–412.

KIRKPATRICK, M.P., WILLIAMSON, N., ARMFIELD, S.W. & ZECEVIC, V. 2020 Destratification of thermally stratified turbulent open-channel flow by surface cooling. *J. Fluid Mech.* **899**, A29.

LARGE, W.G., MCWILLIAMS, J.C. & DONEY, S.C. 1994 Oceanic vertical mixing: a review and a model with a nonlocal boundary layer parameterization. *Rev. Geophys.* **32** (4), 363–403.

DE LAVERGNE, C., MADEC, G., LE SOMMER, J., NURSER, A.J.G. & NAVEIRA GARABATO, A.C. 2015 The impact of a variable mixing efficiency on the abyssal overturning. *J. Phys. Oceanogr.* **46** (2), 663–681.

LEGASPI, J.D. & WAITE, M.L. 2020 Prandtl number dependence of stratified turbulence. *J. Fluid Mech.* **903**.

LEWIN, S.F. & CAULFIELD, C.P. 2021 The influence of far field stratification on shear-induced turbulent mixing. *J. Fluid Mech.* **928**, A20.

LEWIN, S.F. & CAULFIELD, C.P. 2022 Stratified turbulent mixing in oscillating shear flows. *J. Fluid Mech.* **944**, R3.

LUCAS, D., CAULFIELD, C.P. & KERSWELL, R.R. 2017 Layer formation in horizontally forced stratified turbulence: connecting exact coherent structures to linear instabilities. *J. Fluid Mech.* **832**, 409–437.

MAFFIOLI, A., BRETHOUWER, G. & LINDBORG, E. 2016 Mixing efficiency in stratified turbulence. *J. Fluid Mech.* **794**, R3.

MASHAYEK, A., BAKER, L.E., CAEL, B.B. & CAULFIELD, C.P. 2022 A marginal stability paradigm for shear-induced diapycnal turbulent mixing in the ocean. *Geophys. Res. Lett.* **49** (2), e2021GL095715.

MASHAYEK, A., CAULFIELD, C.P. & ALFORD, M.H. 2021 Goldilocks mixing in oceanic shear-induced turbulent overturns. *J. Fluid Mech.* **928**, A1.

MASHAYEK, A. & PELTIER, W.R. 2011 Three-dimensionalization of the stratified mixing layer at high Reynolds number. *Phys. Fluids* **23** (11), 111701.

MASHAYEK, A. & PELTIER, W.R. 2012*a* The 'zoo' of secondary instabilities precursory to stratified shear flow transition. Part 1 Shear aligned convection, pairing, and braid instabilities. *J. Fluid Mech.* **708**, 5–44.

MASHAYEK, A. & PELTIER, W.R. 2012*b* The 'zoo' of secondary instabilities precursory to stratified shear flow transition. Part 2 The influence of stratification. *J. Fluid Mech.* **708**, 45–70.

MASHAYEK, A., SALEHIPOUR, H., BOUFFARD, D., CAULFIELD, C.P., FERRARI, R., NIKURASHIN, M., PELTIER, W.R. & SMYTH, W.D. 2017 Efficiency of turbulent mixing in the abyssal ocean circulation. *Geophys. Res. Lett.* **44** (12), 6296–6306.

MATER, B.D. & VENAYAGAMOORTHY, S.K. 2014*a* The quest for an unambiguous parameterization of mixing efficiency in stably stratified geophysical flows. *Geophys. Res. Lett.* **41** (13), 4646–4653.

MATER, B.D. & VENAYAGAMOORTHY, S.K. 2014*b* A unifying framework for parameterizing stably stratified shear-flow turbulence. *Phys. Fluids* **26** (3), 036601.

MONISMITH, S.G., KOSEFF, J.R. & WHITE, B.L. 2018 Mixing efficiency in the presence of stratification: when is it constant? *Geophys. Res. Lett.* **45** (11), 5627–5634.

ONUKI, Y., JOUBAUD, S. & DAUXOIS, T. 2021 Simulating turbulent mixing caused by local instability of internal gravity waves. *J. Fluid Mech.* **915**, A77.

OSBORN, T.R. 1980 Estimates of the local rate of vertical diffusion from dissipation measurements. *J. Phys. Oceanogr.* **10** (1), 83–89.

POPE, S.B. 2000 *Turbulent Flows*. Cambridge University Press.

PORTWOOD, G.D., DE BRUYN KOPS, S.M. & CAULFIELD, C.P. 2019 Asymptotic dynamics of high dynamic range stratified turbulence. *Phys. Rev. Lett.* **122** (19), 194504.

RILEY, J.J., METCALFE, R.W. & WEISSMAN, M.A. 1981 Direct numerical simulations of homogeneous turbulence in density-stratified fluids. *AIP Conf. Proc.* **76** (1), 79–112.

ROEKEL, L.V., ADCROFT, A.J., DANABASOGLU, G., GRIFFIES, S.M., KAUFFMAN, B., LARGE, W., LEVY, M., REICHL, B.G., RINGLER, T. & SCHMIDT, M. 2018 The KPP boundary layer scheme for the ocean: revisiting its formulation and benchmarking one-dimensional simulations relative to LES. *J. Adv. Model. Earth Syst.* **10** (11), 2647–2685.

SALEHIPOUR, H., CAULFIELD, C.P. & PELTIER, W.R. 2016 Turbulent mixing due to the Holmboe wave instability at high Reynolds number. *J. Fluid Mech.* **803**, 591–621.

SALEHIPOUR, H. & PELTIER, W.R. 2015 Diapycnal diffusivity, turbulent Prandtl number and mixing efficiency in Boussinesq stratified turbulence. *J. Fluid Mech.* **775**, 464–500.

SALEHIPOUR, H. & PELTIER, W.R. 2019 Deep learning of mixing by two 'atoms' of stratified turbulence. *J. Fluid Mech.* **861**, R4.

SALEHIPOUR, H., PELTIER, W.R. & MASHAYEK, A. 2015 Turbulent diapycnal mixing in stratified shear flows: the influence of Prandtl number on mixing efficiency and transition at high Reynolds number. *J. Fluid Mech.* **773**, 178–223.

SCHAAD, S.M. & VENAYAGAMOORTHY, S.K. 2017 Direct numerical simulations of stably stratified decaying unforced turbulence. *Comput. Fluids* **158**, 2–10.

SHIH, L.H., KOSEFF, J.R., FERZIGER, J.H. & REHMANN, C.R. 2000 Scaling and parameterization of stratified homogeneous turbulent shear flow. *J. Fluid Mech.* **412**, 1–20.

SHIH, L.H., KOSEFF, J.R., IVEY, G.N. & FERZIGER, J.H. 2005 Parameterization of turbulent fluxes and scales using homogeneous sheared stably stratified turbulence simulations. *J. Fluid Mech.* **525**, 193–214.

SMYTH, W.D. & MOUM, J.N. 2000 Length scales of turbulence in stably stratified mixing layers. *Phys. Fluids* **12** (6), 1327–1342.

SMYTH, W.D., MOUM, J.N. & CALDWELL, D.R. 2001 The efficiency of mixing in turbulent patches: inferences from direct simulations and microstructure observations. *J. Phys. Oceanogr.* **31** (8), 1969–1992.

VANDINE, A., PHAM, H.T. & SARKAR, S. 2021 Turbulent shear layers in a uniformly stratified background: DNS at high Reynolds number. *J. Fluid Mech.* **916**, A42.

VENAYAGAMOORTHY, S.K. & KOSEFF, J.R. 2016 On the flux Richardson number in stably stratified turbulence. *J. Fluid Mech.* **798**, R1.

WAITE, M.L. & SMOLARKIEWICZ, P.K. 2008 Instability and breakdown of a vertical vortex pair in a strongly stratified fluid. *J. Fluid Mech.* **606**, 239–273.

WILLIAMSON, N., ARMFIELD, S.W., KIRKPATRICK, M.P. & NORRIS, S.E. 2015 Transition to stably stratified states in open channel flow with radiative surface heating. *J. Fluid Mech.* **766**, 528–555.

YI, Y.R. & KOSEFF, J.R. 2022 Dynamics and energetics underlying mixing efficiency in homogeneous stably stratified turbulence. *Phys. Rev. Fluids* **7** (8), 084801.

ZHANG, X., DHARIWAL, R., PORTWOOD, G., DE BRUYN KOPS, S.M. & BRAGG, A.D. 2022 Analysis of scale-dependent kinetic and potential energy in sheared stably stratified turbulence. *J. Fluid Mech.* **946**, A6.

ZHOU, Q., TAYLOR, J.R. & CAULFIELD, C.P. 2017 Self-similar mixing in stratified plane Couette flow for varying Prandtl number. *J. Fluid Mech.* **820**, 86–120.